https://doi.org/10.5194/egusphere-2025-99
Preprint. Discussion started: 28 January 2025

Mesoscale dynamics of an intrathermocline eddy in the Canary Eddy Corridor

Luis P. Valencia[1], Ángel Rodríguez-Santana[1], Borja Aguiar-González[1], Javier Arístegui[2], Xosé A. Álvarez-Salgado[3], Josep Coca[4], and Antonio Martínez-Marrero[2]

[1]University Institute for Research in Sustainable Aquaculture and Marine Ecosystems (IU-ECOAQUA), University of Las Palmas de Gran Canaria (ULPGC), Las Palmas, Spain
[2]Institute of Oceanography and Global Change (IOCAG), University of Las Palmas de Gran Canaria (ULPGC), Las Palmas, Spain
[3]Institute of Marine Research, Spanish National Research Council (CSIC), Vigo, Spain
[4]Cartográfica de Canarias S.A. (GRAFCAN), Las Palmas de Gran Canaria, Spain

Correspondence: Luis P. Valencia (luis.valencia102@alu.ulpgc.es)

Abstract. High-resolution observations of an intrathermocline eddy were conducted in November 2022 within the Canary Eddy Corridor. Formed in early summer 2022, this mature mesoscale eddy exhibited a 550 m vertical extent, with its core centered at 110 m depth, and a segmented horizontal structure with a 25 km inner core radius surrounded by a 55 km-wide outer ring. Propagating southwest at 4.7 km·day^{-1}, its motion aligned with the phase speed of a first-mode baroclinic Rossby wave. Its rotational dynamics featured a 3.9-day inner core rotation period shaped by stratification, which created distinct rotational layers. Rossby number (-0.5) and potential vorticity ($\sim 10^{-11}$ m^{-1}·s^{-1}, 90% less than its surroundings) metrics revealed a core regime dominated by planetary rotation and strong homogeneous water mass isolation, while Burger numbers (length-scale: 0.16; energy-based: 0.68) emphasized the role of stratification and buoyancy forces in shaping its structure. The eddy carried available heat and salt anomalies of 7.052 EJ and 0.016 Tkg, driving heat and salt (freshwater equivalent) fluxes of 5.13 TW and 0.47 Gkg·s^{-1} (-0.013 Sv), underscoring its significance in transporting coastal upwelling waters into the ocean interior. The intrathermocline nature of the eddy developed during the growth phase, and was shaped by surface convergence enhanced by upwelling filament interactions, followed by isopycnal deepening offshore. Throughout its year-long lifespan, the eddy experienced intrinsic instabilities and eddy-to-eddy interactions, culminating in its decay by early summer 2023. The distinct properties of this eddy, alongside the apparent variability of similar features in the Canary Eddy Corridor, underline the need for expanded high-resolution studies, including comprehensive observational efforts and advanced numerical simulations, to better understand their role as zonal pathways for heat, salt, and potentially biogeochemical properties within regional ocean circulation.

1 Introduction

Mesoscale activity in the central portion of the Canary Upwelling System (cCANUS, 25–30°N) is characterized by mesoscale eddies, upwelling fronts, and filaments, which are defining features of this Eastern Boundary Upwelling System (EBUS) (Arístegui et al., 1997; Sangrà et al., 2009; Pacheco et al., 2001; Marchesiello and Estrade, 2009; Hernández-Hernández et al.,

https://doi.org/10.5194/egusphere-2025-99
Preprint. Discussion started: 28 January 2025

2020). Similar to other EBUS, mesoscale variability in this region is driven by instabilities that develop along the transition zone between the coastal upwelling jet and the open ocean flow within the northwest African upwelling system (e.g., Barton et al., 1998; Pelegrí et al., 2005; Benítez-Barrios et al., 2011; Ruiz et al., 2014). Additionally, the presence of islands and archipelagos in cCANUS provides a supplementary mechanism for generating and transforming mesoscale phenomena (e.g., Barton, 2001; Caldeira et al., 2014; Ruiz et al., 2014; Cardoso et al., 2020).

The Canary Archipelago (∼28°N) is a key topographic feature within cCANUS, significantly contributing to the generation of mesoscale structures that form offshore (e.g., Arístegui et al., 1994, 1997; Sangrà et al., 2009). The islands act as topographic barriers, obstructing the southwestward flow of the Canary Current (CC) and the Trade Winds (La Violette, 1974; Van Camp et al., 1991; Hernández-Guerra et al., 1993; Arístegui et al., 1994, 1997; Basterretxea et al., 2002). As a result, mesoscale eddies are generated and detached in a Von Kármán street pattern, propagating southwest of the archipelago (e.g., Chopra and Hubert, 1965; Chopra, 1973; Barton, 2001).

In the wake of the islands, wind shear imparts additional momentum and vorticity to the CC outflow, enabling the detachment of eddies even under relatively weak CC flow (Sangrà et al., 2005, 2007; Jiménez et al., 2008; Piedeleu et al., 2009). These detached eddies typically have lifespans of at least three months, propagate southwestward, and travel thousands of kilometers from their origin (Pingree, 1996; Pingree and Garcia-Soto, 2004; Sangrà et al., 2005, 2007, 2009; Barceló-Llull et al., 2017a). This dynamic process defines the Canary Eddy Corridor (CEC) (Sangrà et al., 2009), a permanent feature of cCANUS that provides a pathway for transporting the physical and biogeochemical properties of water masses from this EBUS into the oligotrophic ocean interior.

The CEC extends from 22°N to 29°N and is predominantly populated by long-lived anticyclonic eddies (AEs) generated south of Tenerife and Gran Canaria islands (Sangrà et al., 2005, 2007, 2009). The dominance of these AEs has been extensively documented through a combination of in situ and satellite observations (Pingree, 1996; Pingree and Garcia-Soto, 2004; Sangrà et al., 2009), as well as various eddy detection and tracking methods (Chaigneau et al., 2009; Sangrà et al., 2009; Mason et al., 2014). Notably, Pegliasco et al. (2015) reported that 40% of the long-lived AEs within the CEC exhibit subsurface intensification, with warm and salty anomalies extending to depths of up to 800 m.

Subsurface-intensified mesoscale AEs, also referred to as intrathermocline eddies (ITEs), are characterized by a lens-shaped core located at subsurface depths within the thermocline (Dugan et al., 1982; Kostianoy and Belkin, 1989; Armi and Zenk, 1984). Their typical structure includes dome-shaped isopleths at the upper boundary and bowl-shaped isopleths at the lower boundary, enclosing a relatively homogeneous core (pycnostad) with properties similar to the water masses at their formation site (e.g., Dugan et al., 1982; Armi and Zenk, 1984; Shapiro and Meschanov, 1991; Gordon et al., 2002; Johnson and Mctaggart, 2010; Hormazabal et al., 2013; Thomsen et al., 2016).

As these eddies propagate into the ocean interior, they induce significant hydrographic and biogeochemical anomalies relative to surrounding waters (e.g., Chaigneau et al., 2011; Pegliasco et al., 2015; Cornejo D'Ottone et al., 2016; Machín and Pelegrí, 2016; Barceló-Llull et al., 2017b; Karstensen et al., 2017). The intensity of these anomalies depends on the integrity of the core during propagation. A useful proxy indicator of this is the non-linearity parameter (ϑ), defined as: $\vartheta = \frac{U_{\max}}{c}$, where $U_{\max}$ is the maximum circum-averaged speed of the eddy and c its translational speed. Non-linearity is characterized by $\vartheta > 1$,

https://doi.org/10.5194/egusphere-2025-99
Preprint. Discussion started: 28 January 2025

indicating trapped waters within the eddy, while highly non-linear eddies exhibit $\vartheta > 5$, with extreme cases exceeding 10 (Chelton et al., 2011).

The ability to trap water is intrinsically linked to the core structure, where the pycnostad reduces static stability, generating large negative anomalies in potential vorticity (PV) (e.g., Nauw et al., 2006; Johnson and Mctaggart, 2010; Pidcock et al., 2013; Barceló-Llull et al., 2017b). These PV anomalies, driven by diminished stratification within the core, enhance the eddy's capacity to isolate and transport water masses, reinforcing the relationship between non-linearity, vorticity, and the homogeneous water properties of ITEs.

Observational evidence confirms the presence of ITEs in many regions of the world's oceans. However, comprehensive studies on their formation and early evolution are still limited (Caldeira et al., 2014), and most of the current knowledge comes from numerical simulations under both realistic and idealized oceanic conditions. Thus, understanding the origin of ITEs remains an active area of research.

Hogan and Hurlburt (2006) identified three non-exclusive mechanisms of ITE formation in a realistically simulated Japan/East Sea:

1. advection of stratified water capping a pre-existing anticyclone,
2. restratification of the upper layers in a pre-existing anticyclone due to seasonal heating or cooling, and
3. frontal convergence and subduction of winter surface mixed layer water.

Frontal convergence and subduction have also been proposed as the formation mechanism for ITEs in the Southern Indian Ocean by Nauw et al. (2006). Further insights on frontal subduction as a source for ITE core waters were provided by Thomas (2008), who concluded that winds blowing in the direction of a frontal jet reduce the PV of waters through friction. Vertical circulation driven by frontal meanders subsequently subducts these low-PV waters into the pycnocline, forming ITEs.

In the California and Peru-Chile upwelling systems, recent studies have explored the role of frictional forces exerted by continental slope topography on poleward undercurrents, leading to the formation of Slope Water Oceanic Eddies (Molemaker et al., 2015; Contreras et al., 2019). Locally induced mechanisms, such as the transformation of a surface AE into an ITE through eddy-wind interactions, have also been proposed. For example, Mcgillicuddy (2015) suggested that local Ekman suction within the AE can drive upwelling strong enough to dome the seasonal thermocline, converting the surface AE into an ITE.

In the cCANUS, observational evidence of ITEs primarily pertains to Mediterranean Water lenses (meddies) (e.g., Armi and Zenk, 1984; Richardson et al., 2000; Machín and Pelegrí, 2016). Instabilities in the outflow of the Mediterranean Undercurrent generate these structures, and they are characterized by strong positive salinity and temperature anomalies with thicknesses of 500–1000 m, typically centered at intermediate depths (∼1000 m). Their lifespans range from one to three years and they can travel thousands of kilometers southwestward before their cores erode through lateral mixing or salt-fingering double diffusion processes (Ruddick and Hebert, 1988; Hebert et al., 1990; Schultz Tokos and Rossby, 1991), or abruptly collapse due to interactions with rough topography (Richardson et al., 1989).

https://doi.org/10.5194/egusphere-2025-99
Preprint. Discussion started: 28 January 2025

Shallower ITEs, centered within the upper 500 m of the water column, have also been observed in cCANUS. Pingree (1996) provided the first detailed description of a long-lived AE centered at 190 m depth. This AE, with a diameter of ∼100 km and a vertical extent of ∼150 m, was named *Flatty* due to its low aspect ratio. Nearly a year after its formation, Flatty had traveled approximately 1600 km from its origin in the CEC.

In 2014, using remote sensing and in situ data, Caldeira et al. documented the formation of a wind-induced ITE in the lee of Madeira Islands. The ITE was centered at ∼100 m depth and characterized by a 25 km radius, 100 m width, and a translational speed of 5 km $\cdot$ day^{-1}. More recently, Barceló-Llull et al. (2017b) studied the anatomy of the ITE *PUMP*, which formed in the lee of Tenerife Island and exhibited a 46 km radius and a 500 m vertical extent, with two low-PV cores located at 85 m and 225 m depth, when surveyed four months after its formation and 550 km from its origin.

In November 2022, an AE originating in the lee of Gran Canaria Island in June 2022 (five months prior) was thoroughly sampled south of the Canary Archipelago. This eddy, named *Bentayga*, displayed the subsurface intensification typical of an ITE and shared broad similarities in formation, location, and timing with other documented eddies. Despite the similarities, it displayed remarkable hydrographic and dynamic differences, highlighting the complexity and variability inherent to these systems. Moreover, these differences emphasize the importance of cautious interpretation of findings to prevent overgeneralizing eddy dynamics to the entire population of ITEs within the CEC.

The current study integrates satellite observations with in situ measurements to investigate the formation and evolution of the Bentayga eddy in the CEC. The primary objective is twofold: (1) to explore the mechanisms responsible for the eddy's formation; and (2) to evaluate its influence on the physical properties of the regional ocean circulation. Additionally, the study compares the ITE with similar structures both within the CEC and in other regions of the world, offering new insights into the complexity and variability of mesoscale eddy activity.

The structure of this manuscript is as follows: Sect. 2 describes the survey, datasets, and methodology; Sect. 3 presents the results, including a Lagrangian analysis of the eddy's geometric properties and two- and three-dimensional analyses of circulation dynamics; Sect. 4 discusses the findings in comparison to other intrathermocline eddies; and concluding remarks are presented in Sect. 5.

2 Data and methods

2.1 Survey description

An interdisciplinary oceanographic survey was conducted aboard the R/V *Sarmiento de Gamboa* from 9 November to 4 December 2022, as part of the *Biogeochemical Impact of Mesoscale and Sub-mesoscale Processes Along the Life History of Cyclonic and Anticyclonic Eddies* (eIMPACT) project. This survey, called the eIMPACT2 survey, targeted a mature AE which originated southwest of Gran Canaria Island (GCI). The eddy has been named Bentayga, inspired by the Saharan-Berber heritage of the Canarian aborigines, reflecting its connection to Saharan upwelling waters off the northwest African coast. At the time of the survey, it was approximately 4.5 months old and had traveled 560 km from its formation site (Fig. 1).

https://doi.org/10.5194/egusphere-2025-99
Preprint. Discussion started: 28 January 2025

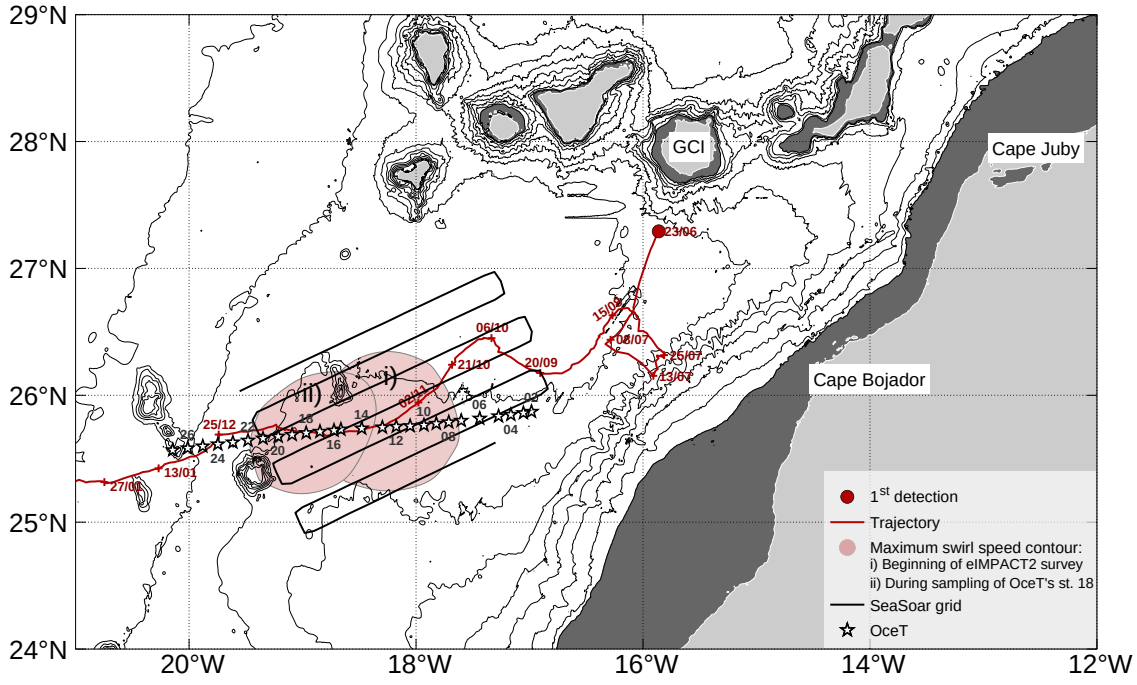

Figure 1. Map of the study area, the Canary Eddy Corridor (CEC), during the eIMPACT2 survey (9 November–4 December 2022). Land and the continental shelf (seafloor depths between 0 and 200 m) are shown in light and dark grey for the Canary Islands and the northwestern African coast, respectively. Isobaths are displayed every 500 m, ranging from 500 to 5000 m depth (thin black contours). The thick black line represents the ship's grid-like trajectory during the eIMPACT2 SeaSoar phase (9–14 November). White stars indicate the locations of stations from the oceanographic transect (OceT, 19–28 November). The eddy is depicted by its position at first detection (dark red circle), its trajectory (thick dark red line with dates), and areas enclosed by the contour of maximum velocity at: (i) the start of the eIMPACT2 survey (9 November) and (ii) sampling at OceT station 18 (25 November), shown as light red patches.

Continuous *yo-yo* tows of a CTD-O (*Conductivity, Temperature, Depth - Oxygen*; *Sea-Bird* SBE911plus) mounted on an undulating vehicle (SeaSoar Mk II; *Chelsea Technologies Group*), combined with VMADCP (*Vessel-Mounted Acoustic Doppler Current Profiler*; *RDI* Ocean Surveyor, 75 kHz) measurements, were conducted during the eIMPACT2 SeaSoar phase (9–14 November 2022) to construct three-dimensional hydrographic and dynamical fields of the eddy and its surroundings. This phase employed a southwest–northeast sampling grid comprising seven transects (278 km each), separated by ∼22 km, and sampled vertical levels between 30 and 320 m. A total of 955 CTD-O casts were recorded, with an average horizontal spacing of ∼2 km. Continuous VMADCP measurements were collected in parallel along the grid.

Another phase used in this study, the eIMPACT2 OceT phase (19–28 November 2022), involved vertical CTD-O profiles along a nearly zonal transect (OceT) crossing the eddy from east to west. This transect included 26 stations (stations 02–27),

https://doi.org/10.5194/egusphere-2025-99
Preprint. Discussion started: 28 January 2025

spaced 12.7 ± 2.8 km apart, and extended from the surface to ∼1500 m depth (Fig. 1). Alongside these profiles, continuous VMADCP velocities spanning ∼30–800 m depth were recorded throughout the transect.

Raw CTD-O data from both phases were processed at 1-meter intervals using the manufacturer's software, and TEOS-10 algorithms were applied to compute derived variables such as absolute salinity (S_A), conservative temperature (Θ), potential density anomaly (σ_θ), and Brunt-Väisälä frequency (N) (Feistel, 2003, 2008). VMADCP data were processed with CODAS software (https://currents.soest.hawaii.edu/docs/adcp_doc/), resulting in 16-meter vertical bins for both phases (Martínez-Marrero et al., 2019).

To reduce noise in the OceT data, a two-dimensional Gaussian filter with horizontal and vertical scales of 12 km and 8 m, respectively, was applied to minimize the influence of unresolved short-scale fluctuations. For the SeaSoar phase, CTD-O and VMADCP datasets were objectively interpolated onto a regular 11 × 11 km grid at 16-meter VMADCP levels. This process assumed planar mean CTD variables and constant mean VMADCP velocities (Rudnick and Luyten, 1996), employing a circular Gaussian covariance model with a 44 km scale ($L_x = L_y$), approximating the theoretical Rossby radius (Chelton et al., 1998), and incorporating 3% uncorrelated noise in the final fields (Bretherton et al., 1976, 1984; Le Traon, 1990).

2.2 Satellite information and derived products

The Atlas of Mesoscale Eddy Trajectories (META3.2exp NRT), developed by SSALTO/DUACS and distributed by AVISO+ with the support of CNES, in collaboration with IMEDEA (Pegliasco et al., 2022) (https://www.aviso.altimetry.fr/), was used to track, from its formation to dissipation, the geometric and dynamic properties of the Bentayga eddy. The atlas is based on the detection and tracking of mesoscale eddies globally using altimetry data from multiple platforms, applying the eddy detection method of Mason et al. (2014) to provide daily information on the location, speed, radius, and other features of detected eddies, classifying them by gyre type (CE and AE). The dataset spans from 2018 to the present, with a 15-day delay. This information was complemented with sea level anomaly fields (relative to the average field for the period 1993–2012) and geostrophic current fields from the European Seas Gridded L4 Sea Surface Heights and Derived Variables NRT altimetry product. This product, with a spatial resolution of 0.125° × 0.125°, is processed by the multi-platform altimetry data system DUACS and distributed by the E.U. Copernicus Marine Service Information (https://doi.org/10.48670/moi-00142).

To characterize the interaction between the circulation driven by this eddy and the upwelling fronts and filaments off the northwest African coast, we used daily fields of Sea Surface Temperature (SST) from the GHRSST Level 4 MUR Global Foundation Sea Surface Temperature Analysis product. This dataset, with a resolution of 1 km × 1 km, is distributed by PO.DAAC (https://doi.org/10.5067/GHGMR-4FJ04). In addition, satellite chlorophyll-a data, with a resolution of 4 km × 4 km, were obtained from the Global Ocean Colour (Copernicus-GlobColour) Bio-Geo-Chemical Level 3 product distributed by the E.U. Copernicus Marine Service Information (https://doi.org/10.48670/moi-00280). Both of these products are derived from a combination of satellite information from all available platforms, utilizing specific processing, analysis, and merging schemes (Chin et al., 2017; Garnesson et al., 2019).

https://doi.org/10.5194/egusphere-2025-99
Preprint. Discussion started: 28 January 2025

2.3 Dynamical properties

2.3.1 Potential vorticity

As mentioned in Sect. 1, a key signature of ITEs is their core of low PV, resulting from the nearly homogeneous waters they contain. Given the geometry of the Bentayga eddy, the following form of Ertel's PV (Müller, 1995) was employed:

$$PV = -\frac{(-\partial_z v, \partial_z u) \cdot \nabla_h \sigma_\theta}{\rho_0} - \frac{(\zeta + f)\partial_z \sigma_\theta}{\rho_0} \quad (1)$$

This expression includes two sources of PV : the first term on the right-hand side represents PV associated with isopycnal tilting, while the second term corresponds to PV due to water column stretching. In the first term, $(-\partial_z v, \partial_z u)$ is the vertical shear of the horizontal velocity vector (u, v), and $\nabla_h \sigma_\theta$ is the horizontal gradient of the potential density anomaly (σ_θ). In the second term, $(\zeta + f)$ is the absolute vorticity, defined as the sum of relative vorticity (ζ) and planetary vorticity (f), while $\partial_z \sigma_\theta$ represents the vertical gradient of σ_θ. For both terms, a mean background density $\rho_0 = 1026$ kg·m^{-3} was used. The calculations were based on the objectively interpolated fields.

2.3.2 Energy metrics

The total Available Potential Energy (APE) and Kinetic Energy (KE) within the eddy were estimated using volume integrals based on the approach of Schultz Tokos and Rossby (1991), applied to the hydrographic and current records collected along the OceT transect. For both integral calculations, the eddy's volume was assumed to be cylindrical and treated as an isolated structure within an infinitely wide ocean basin (Hebert, 1988), where unperturbed hydrographic fields explicitly define the reference ocean state. The estimation of these reference fields is described further in Sect. 3.2. The integrals were performed over the water column, from the surface $(z = 0)$ to the trapping depth $(z = H)$ (e.g., Dilmahamod et al., 2018; Morris et al., 2019), and radially, from its center (r=0) to its outer radius (r=R). The total APE was calculated as follows:

$$APE = 0.5\rho_r \int_H^0 \int_0^R {N_r}^2 \delta^2 (2\pi r) dr dz \quad (2)$$

where ρ_r is the density of the reference state, N_r is the Brunt-Väisälä frequency of the reference state, δ represents the vertical departures of the isopycnal surfaces from the reference state, and $2\pi r dr$ is the infinitesimal area element. The total KE within the eddy was calculated as:

$$KE = 0.5\rho_r \int_H^0 \int_0^R \mathbf{u}^2 (2\pi r) dr dz \quad (3)$$

where **u** denotes the horizontal velocity obtained from the VMADCP.

2.3.3 Thermohaline anomalies

To evaluate the thermohaline perturbations induced by the eddy, the Available Heat Anomaly (AHA) and Available Salt Anomaly (ASA) were calculated following the methodology of Chaigneau et al. (2011). These volume integrals were com-

https://doi.org/10.5194/egusphere-2025-99
Preprint. Discussion started: 28 January 2025

puted under the same assumptions described earlier. However, as in Barceló-Llull et al. (2017a), the radial integration was limited to the inner core radius of the Bentayga eddy (r = R_C; see Sect.s 3.2 and 3.4). The AHA and ASA were calculated as:

$$AHA = \int_{H}^{0} \int_{0}^{R_C} \rho C_p \Theta'(2\pi r) dr dz \tag{4}$$

$$ASA = 0.001 \int_{H}^{0} \int_{0}^{R_C} \rho {S_A}'(2\pi r) dr dz \tag{5}$$

In both equations, ρ represents the potential density. In Eq. 4, C_p is the specific heat capacity, set to 4000 J·kg^{-1}·K^{-1}, while in Eq. 5, the factor 0.001 converts salinity into a fraction of kg of salt per kg of seawater. The conservative temperature (Θ') and absolute salinity (S'_A) anomalies were defined as departures from the same unperturbed reference ocean state used in the calculations of APE and KE (Eq. 2 and Eq. 3).

2.3.4 Eddy-driven fluxes

The volume, heat, and salt transported by the eddy were assessed by estimating the corresponding horizontal eddy-driven fluxes (Dilmahamod et al., 2018). Following the approach of Morris et al. (2019), it was treated as a bulk entity, assuming a vertically constant translational speed (c), calculated as the average speed during the eIMPACT2 survey. The volume (V_e), heat (Q_{eh}), salt (Q_{es}), and freshwater (Q_{fw}) fluxes were calculated as follows:

$$V_e = c \int_{H}^{0} (2r) dz \tag{6}$$

$$Q_{eh} = c \int_{H}^{0} \rho_0 C_p \Theta'(2r) dz \tag{7}$$

$$Q_{es} = 0.001 c \int_{H}^{0} \rho_0 {S_A}'(2r) dz \tag{8}$$

$$Q_{fw} = \frac{-Q_{es}}{\rho_0 S_0} \tag{9}$$

In these equations: V_e represents the eddy-driven volume transport in Sverdrups (1 Sv = 10^6 m^3·s^{-1}), Q_{eh} is the eddy-driven heat flux in Watts (W), Q_{es} is the eddy-driven salt flux in kilograms per second (kg·s^{-1}), and Q_{fw} is the equivalent freshwater flux in Sverdrups. Here, $\rho_0 = 1026$ kg·m^{-3} is the mean background density, $C_p = 4000$ J·kg^{-1}·K^{-1} is the specific heat capacity, and $S_0 = 35$ (dimensionless, representing salt mass fraction in psu) is the mean upper-ocean salinity. Conservative temperature (Θ') and absolute salinity anomalies (${S_A}'$) were calculated as departures from the unperturbed reference state.

https://doi.org/10.5194/egusphere-2025-99
Preprint. Discussion started: 28 January 2025

3 Results

3.1 Lagrangian evolution as seen from satellite altimetry data

The Bentayga eddy formed south of GCI in June 2022, with its first detection recorded on 23 June (Figs. 1–3). Shortly after formation, during its growth phase, it drifted away from GCI almost immediately (see trajectory and respective dates in Figs. 1 and 2). The initial 20 days were characterized by a rapid southwestward movement, which later shifted to an almost eastward direction, with speeds ≥ 10 km $\cdot$ day^{-1}, covering approximately 170 km from the origin to the continental margin of NW Africa, near Cape Bojador ($\sim 26.1°$N).

During this phase, significant growth was observed only in its radius (Fig. 3c). It remained in this region for over two weeks, during which it interacted with upwelling filaments extending from Cape Juby to the north and Cape Bojador to the south (Fig. 2b).

Throughout this period, the sea level anomaly (SLA) amplitude and swirl speed increased considerably, rising by approximately 4 cm and 15 cm$\cdot$s^{-1}, respectively (Figs. 3a, b). This behavior gave a strong non-linear character to the Bentayga eddy, as indicated by $\vartheta > 5$ (Fig. 3e), a feature that persisted throughout the analyzed period. By the end of July, it began to move northwestward into the open ocean, maintaining this trajectory while continuing to exhibit gradual increases in the aforementioned features until 15 August (Figs. 1 and 3).

At this stage, peak values were reached in amplitude ($\sim$20 cm), swirl speed ($\sim$55 cm$\cdot$s^{-1}), radius ($\sim$55 km), and angular velocity ($\sim 11 \times 10^{-6}$ rad$\cdot$s^{-1}) (Figs. 3a–d). These relatively higher values were sustained until the early days of November (Figs. 3a–c), when the temporal evolution of these features displayed a plateau behavior, particularly evident in the SLA amplitude and swirl speed, even after accounting for the 15–30-day fluctuations observed throughout its life cycle (Figs. 3a, b). This plateau indicates that the Bentayga eddy had entered its mature phase by this time, with mean values of approximately $\sim 18 \pm 2$ cm for SLA amplitude, $\sim 45 \pm 4$ cm$\cdot$s^{-1} for swirl speed, and $\sim 50 \pm 5$ km for radius.

The temporal evolution of its angular velocity and non-linear character also evolved into a plateau during this phase (Figs. 3d, e); however, for angular velocity, it persisted only until mid-October, with a mean magnitude of approximately 10^{-5} rad$\cdot$s^{-1}. Throughout this phase, it primarily followed a southwestward trajectory (Figs. 1 and 2c, d), although a northwestward deflection was observed in its path between mid-September and early October (Fig. 1).

Starting in the first weeks of November, a gradual decline in all the previously described properties became evident (Fig. 3) indicating that the eIMPACT2 survey occurred at the onset of this slow decline in the dynamic properties during the eddy's mature phase. Such a smooth and gentle decrease in the magnitude of the eddy's dynamic properties during this phase has been previously observed in the CANUS and other EBUS (Pegliasco et al., 2015).

During the eIMPACT2 survey, the Bentayga eddy moved with a translational speed (c) of 4.5 ± 1.2 km$\cdot$day^{-1} and displayed a mean SLA amplitude of 15 ± 1 cm, swirl speed of 38 ± 2 cm $\cdot$ s^{-1}, radius of 55 ± 3 km, mean angular velocity of $7 \pm 0.3 \times 10^{-6}$ rad $\cdot$ s^{-1}, and a strong non-linear character ($\vartheta > 5$).

A few days after the campaign concluded, the nearly linear decline in these properties was interrupted by shorter-period fluctuations (with a temporal scale of 10–20 days), particularly noticeable in the SLA amplitude and radius. These fluctuations

https://doi.org/10.5194/egusphere-2025-99
Preprint. Discussion started: 28 January 2025

persisted until the end of its mature phase in mid-May 2023 (Figs. 3a, c). It appears that the onset of these shorter-scale fluctuations coincided with a slight northwestward deflection observed in its trajectory (Fig. 1).

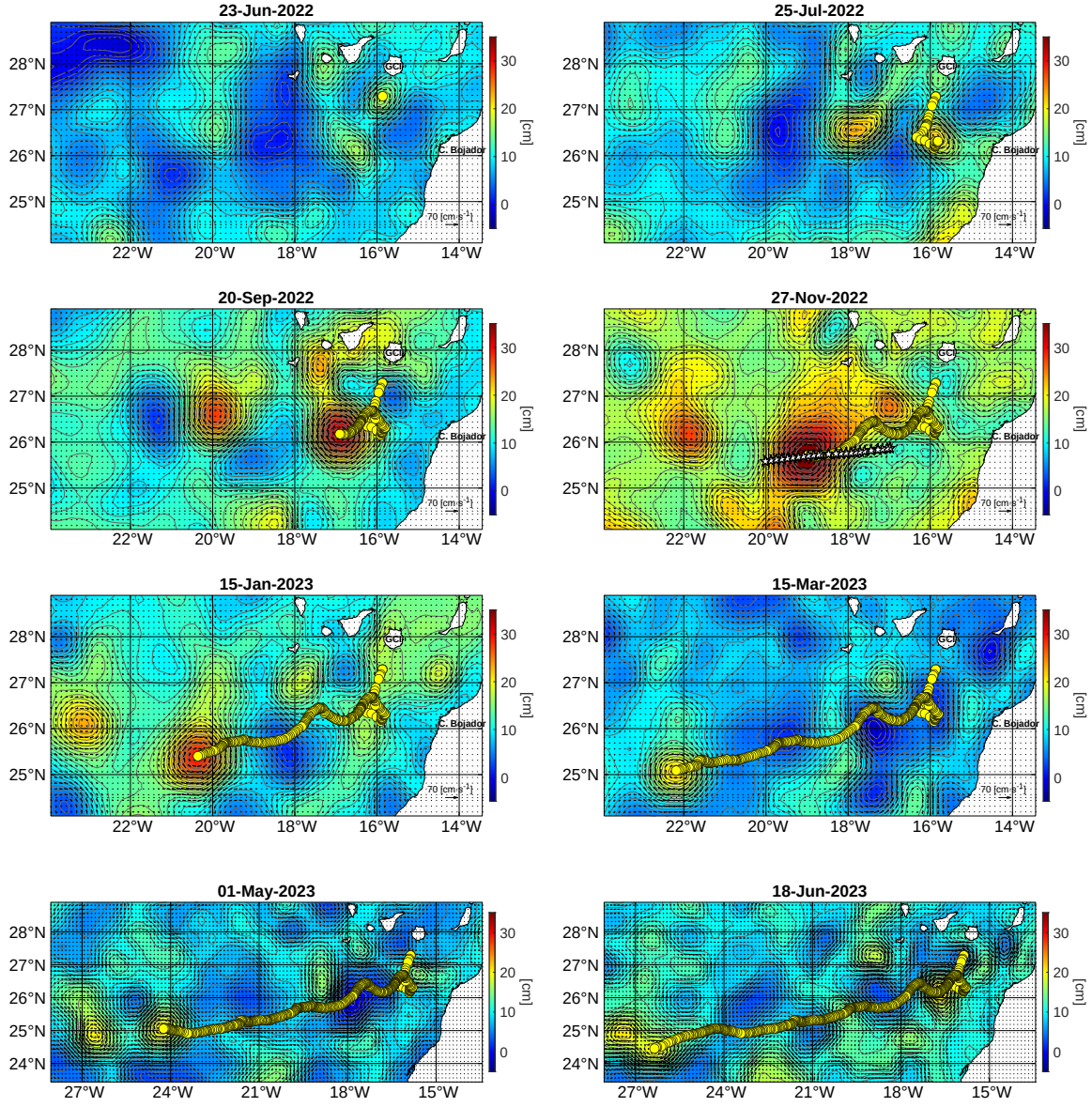

Figure 2. Sea level anomaly snapshots (color map and thin grey contours) and geostrophic currents (black arrows) derived from satellite altimetry. The panels show the eddy's evolution from its first detection on 23 June 2022, through its various phases, including the eIMPACT2 survey, to its dissipation on 18 June 2023 (trajectory indicated by yellow circles). White stars denote oceanographic station locations during the eIMPACT2 OceT phase.

https://doi.org/10.5194/egusphere-2025-99
Preprint. Discussion started: 28 January 2025

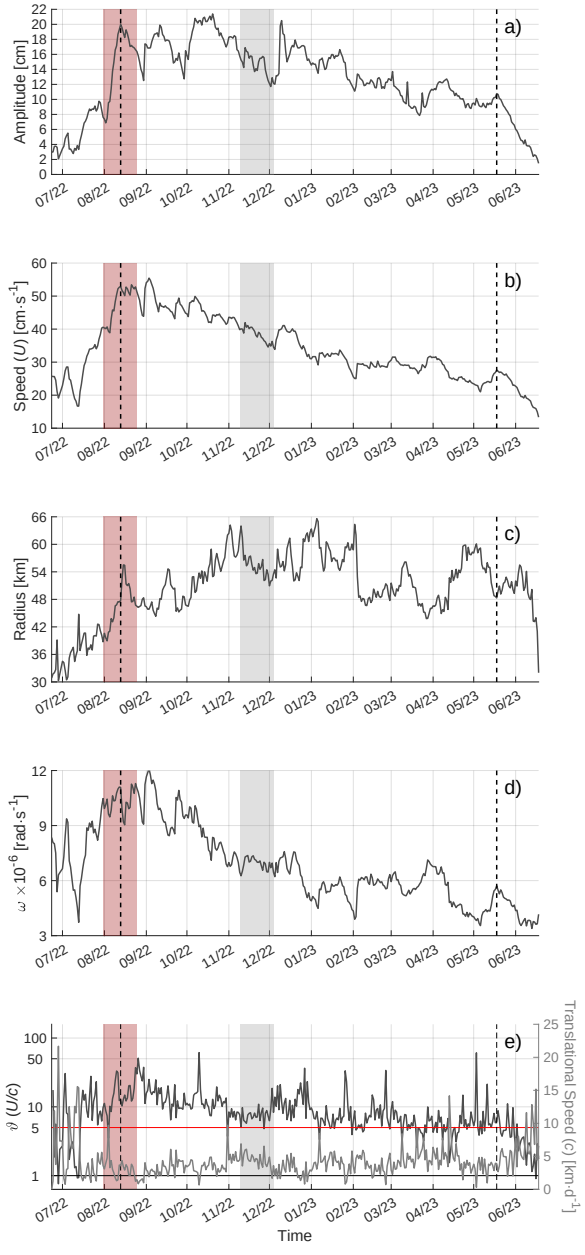

Figure 3. Time series of geometric and dynamic properties of the eddy from its first detection (23 June 2022) to its dissipation (18 June 2023). Panels show: amplitude (a), swirl speed (b), radius (c), angular speed (ω, d; calculated as swirl speed divided by radius), and the non-linearity parameter (ϑ, e; estimated as the ratio of swirl to translational speeds). In panel e, the translational speed is indicated by the grey line, while black and red horizontal lines represent thresholds for non-linearity ($\vartheta > 1$) and strong non-linearity ($\vartheta > 5$) (Chelton et al., 2011). Pale red and grey shaded areas across all panels highlight periods when the eddy was near the NW African continental margin and during the eIMPACT2 survey, respectively. Vertical dashed lines indicate the onset and end of its mature phase. Data were derived from the META3.2 NRT product.

https://doi.org/10.5194/egusphere-2025-99
Preprint. Discussion started: 28 January 2025

Finally, from late May 2023 onward, the dynamical properties of the Bentayga eddy exhibited an abrupt decrease, marking its transition into the decay phase, which culminated in its dissipation on 18 June 2023.

The temporal evolution of the eddy properties was dominated by two main modes of variability (Fig. 3). The first mode was a long-term component, spanning 7–11 months, associated with its overall life cycle: growth (mid-June 2022 to mid-August 2022), maturity (including the slow decline stage; mid-August 2022 to mid-May 2023), and rapid decay (starting in late May 2023) (Fig. 3).

The second mode of variability involved shorter-scale fluctuations, ranging from weeks to a few months, as identified through wavelet analysis (Appendix Fig. A1). Generally, these fluctuations displayed a degree of synchronicity among the analyzed properties, reflecting the dominance of geostrophic characteristics even at these scales. However, the relative energy contributions of these fluctuations did not always align, with greater intensity observed in the variability of the SLA amplitude and radius.

This behavior could be interpreted as a mode of eddy pulsation, similar to that described by Sangrà et al. (2005, 2009), suggesting a connection with changes in Bentayga's elliptical eccentricity and the presence of sharp meanders at its edges. These phenomena are likely due to eddy-to-eddy interactions (Sangrà et al., 2005; Morris et al., 2019) or some form of submesoscale instability (Brannigan et al., 2017).

3.2 Circulation and hydrography

Cross-transect velocities along the OceT (Fig. 4a) were primarily influenced by the anticyclonic circulation induced by the Bentayga eddy (stations 12–24, 120–280 km from OceT's origin). Stronger velocities (>30 cm·s^{-1}) extended from the surface to the σ_θ = 25.5 kg·m^{-3} isopycnal depth, closely following its concave shape. Between stations 15–20 (175–225 km from OceT's origin), higher cross-transect velocities were observed at approximately 110–120 m depth (>45 cm·s^{-1}). However, at station 18, velocities were nearly zero throughout the entire depth profile, indicating proximity to its center (Figs. 4a, b).

Starting from stations 15 and 20 towards the east and west, respectively, the vertical segment of higher velocities became slightly shallower, with stations 12 and 24 roughly marking the eastern and western boundaries of the eddy. This variation in the vertical position of the maximum cross-transect velocity layer suggests the presence of an inner core within, with a radius of 25 km, and an external ring approximately 55 km wide. The external ring spans roughly between stations 20 and 24 to the west, and stations 12 and 15 to the east, with its lower (deeper) limits closely following the spatial behavior of the aforementioned isopycnal (Fig. 4a). Vertical profiles of cross-transect velocity (Fig. 4b) reveal a slight horizontal tilt, with stronger velocities occurring at deeper depths within the inner core, and at shallower depths in the outer ring (Figs. 4a, b). A more detailed analysis of the external ring, however, indicates that it is not spatially homogeneous (Fig. 4).

Specifically, the external ring can be divided into two distinct regions, particularly noticeable within the upper 70 m of the water column. The inner segment of this external ring, spanning a radius of approximately 65 km from the center of the eddy, is characterized by a radial increase in cross-transect (azimuthal) velocity, observed roughly between stations 20 and 23 to the west, and stations 13 and 15 to the east. Beyond this, the outer segment of the ring extends outward by an additional 15 km (up

https://doi.org/10.5194/egusphere-2025-99
Preprint. Discussion started: 28 January 2025

to a total radius of 80 km) and displays a gradual radial decrease in velocity. This outer segment is evident between stations 23 and 24 to the west, and stations 12 and 13 to the east.

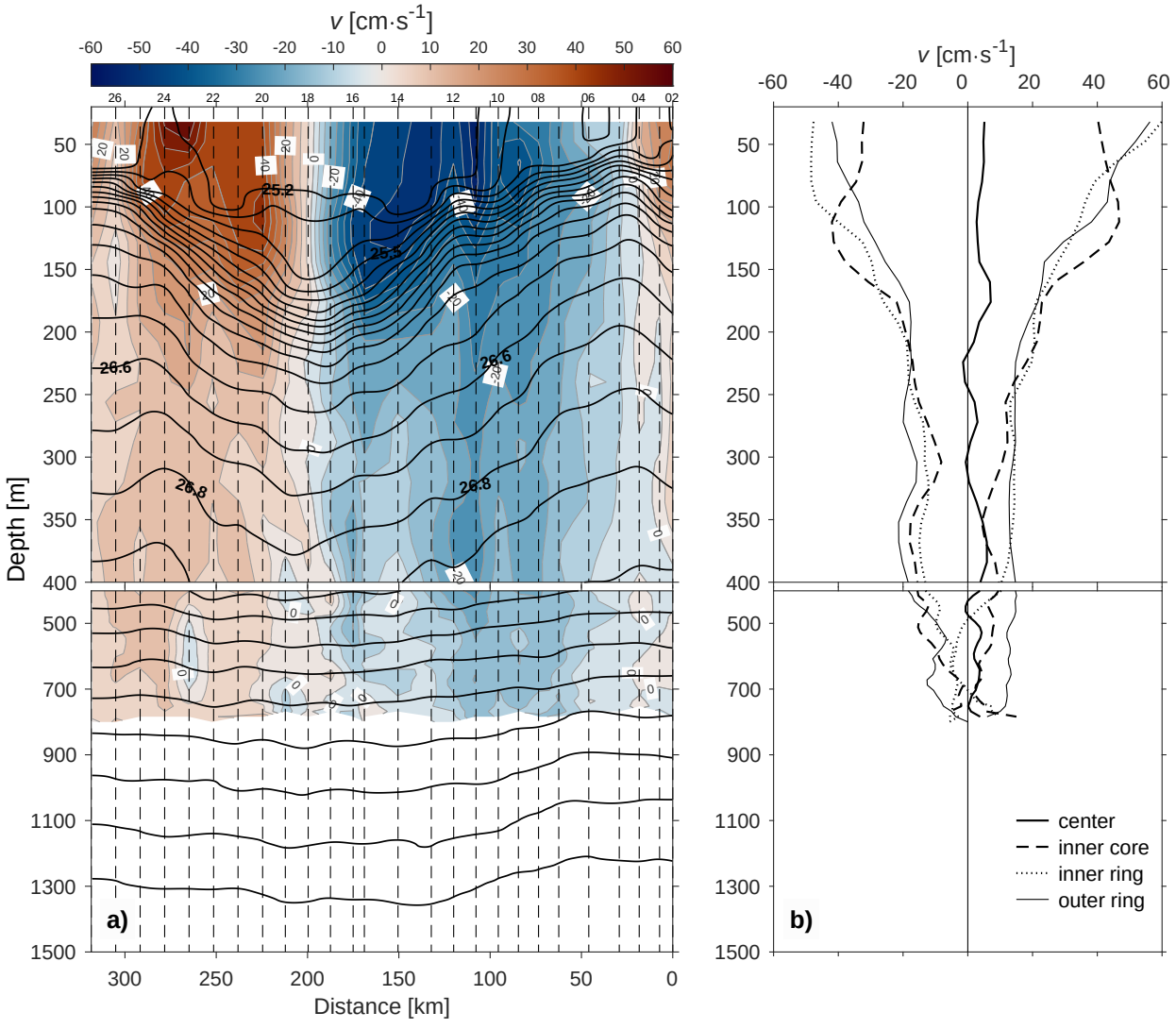

Figure 4. a) Vertical section of cross-transect velocities (v) from VMADCP measurements along the OceT transect. Grey contours represent velocity levels at 5 cm·s^{-1} intervals, while black contours show isopycnals (σ_θ) ranging from 25.2 to 27.7 kg·m^{-3} with 0.1 kg·m^{-3} intervals. Vertical dotted lines indicate the positions of oceanographic stations, with only even station numbers labeled for clarity. b) Vertical profiles of cross-transect velocities at the eddy's center (station 18), inner core (stations 16 and 20), inner ring (stations 13 and 23), and outer ring (stations 12 and 24) (refer to text for further details). Different vertical scales are applied for the 0–400 m and 400–1500 m depth ranges in both panels.

https://doi.org/10.5194/egusphere-2025-99
Preprint. Discussion started: 28 January 2025

This dual structure within the outer ring adds complexity to the overall azimuthal velocity distribution, highlighting radial variations that could impact the stability and mixing properties of the Bentayga eddy (McWilliams, 1985). These circulation patterns remained spatially coherent above the σ_θ = 26.6 kg·m^{-3} isopycnal. However, at greater potential density anomalies (26.7–27.4 kg·m^{-3}), the anticyclonic circulation weakened (<15 cm·s^{-1}) and became more spatially disordered. Outside its outer boundaries, cross-transect velocities aligned with the external cyclonic circulation observed on either side (Fig. 2d).

From Fig. 5a, the deepening of the isopycnal surfaces is evident for $\sigma_\theta \geq 25.4$ kg·m^{-3} between stations 12 and 24, with the seasonal pycnocline (associated with N values ≥ 5 cph) exhibiting a concave shape along this horizontal segment. In contrast, lighter isopycnals displayed a slight convex shape between stations 15 and 20 (175–225 km from OceT's eastern origin) along the $\sigma_\theta = 25.2$ kg·m^{-3} isopycnal. The presence of a deep surface mixed layer (extending from the surface to a depth of 80 m), containing even lighter waters (< 25.2 kg·m^{-3}), along with a shallower and less intense pycnocline (with N values of 3–4 cph), likely prevented doming of these lighter isopycnals.

The core of the Bentayga eddy was centered between these shallower and deeper pycnoclines ($\sim$110 m depth), enclosing nearly homogeneous water and forming a pycnostad with a mean potential density anomaly of 25.3 ± 0.05 kg·m^{-3}. As expected, outside the influence of the eddy (westward from station 24 and eastward from station 12), the density field was influenced by the cyclonic circulation on both sides, with a mesoscale elevation of water (isopycnal lifting) noticeable even at depths around 500 m (Fig. 5a).

Most of the structures for the distribution of σ_θ along the OceT described above are also observed in the first 600 m of the vertical sections of Θ and S_A (Fig. 5b, c). Between stations 12 and 24, the 12.5–22°C isotherms and 36–36.9 g·kg^{-1} isohalines exhibited the previously mentioned deepening. Signs of minor elevation in the horizontal segment between stations 15 and 20 were also noticeable along the 23°C isotherm and the 36.9 g·kg^{-1} isohaline, as well as a core of nearly constant temperature and salinity, with mean values of 22.5 ± 0.2°C and 36.83 ± 0.01 g·kg^{-1}.

The inner core was vertically bounded by two sharp positive thermoclines ($\sim$0.1°C·m^{-1}), a sharp positive upper halocline (0.02 g·kg^{-1}·m^{-1}), and a weaker negative lower halocline (-0.01 g·kg^{-1}·m^{-1}). In the S_A field, the structure of the eddy core was more clearly defined by the 36.8 g·kg^{-1} isohaline, forming a bag-like shape of relatively fresher water compared to the surrounding waters at the same vertical levels. It is important to note that, aside from the mesoscale perturbations in the thermohaline properties along the OceT, their overall hydrographic distribution corresponded to the expected water mass composition for the region, with a dominance of 12° and 15°C Eastern North Atlantic Central Waters (ENACW12 and ENACW15, respectively) (Fig. 6).

At intermediate depths (700–1300 m), relatively colder and fresher waters were observed from station 7 westward (approximately 60 km from OceT's origin) (Fig. 5b, c). These waters were consistent with the thermohaline values and the higher contribution of the diluted Antarctic Intermediate Water (AAIW) previously described in this region at these depths (Alvarez et al., 2005; Bashmachnikov et al., 2015; Jiménez-Rincón et al., 2023). In this study, the acronym AA, from the nomenclature proposed by Alvarez et al. (2005), will be used to refer to this water mass, as its thermohaline properties align with those observed locally in this region (Fig. 6), albeit with slight variations from the classical definition of AAIW (Tomczak and Godfrey,

https://doi.org/10.5194/egusphere-2025-99
Preprint. Discussion started: 28 January 2025

2004). No disturbances in the σ_θ field were observed despite these changes, indicating that density remained compensated (Fig. 5a).

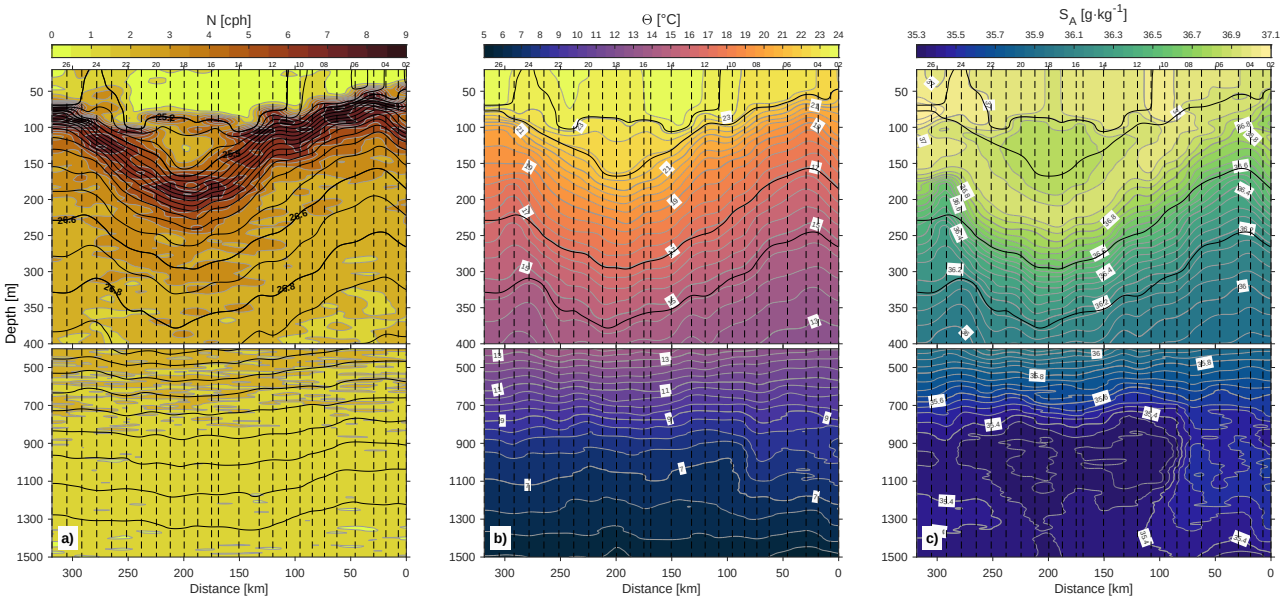

Figure 5. Vertical sections along the OceT of: a) Brunt-Väisälä frequency (N), b) conservative temperature (Θ), and c) absolute salinity (S_A). In panel (a), black contours represent isopycnals (σ_θ) ranging from 25.2 to 27.7 kg·m^{-3}, with a contour interval of 0.1 kg·m^{-3}. In panels (b) and (c), thick black contours correspond to σ_θ levels of 25.2, 25.5, 26.6, and 26.8 kg·m^{-3}. Vertical dotted lines indicate the positions of oceanographic stations as shown in Fig. 4A. Consistent with Fig. 4, different vertical scales were applied for the 0–400 m and 400–1500 m depth ranges.

This compensation may also explain the localized enrichment of thermohaline fine structure, likely due to lateral intrusions, which were more noticeable in the S_A field (Fig. 5c). Additionally, within the area thought to be influenced by the Bentayga eddy (stations 12–24), the relative contribution of AA appeared stronger and was accompanied by a higher presence of Sub-Polar Mode Water (SPMW) above it (Fig. 5b, c; Fig. 6). This suggests a possible connection between the anticyclonic circulation driven by the eddy and the vertical extent of its trapping capacity (i.e., its non-linearity ratio, ϑ, see Fig. 3e). However, as explained in Sect. 2.1, reliable VMADCP velocity records were not obtained for these depths, preventing further analyses.

To further investigate the impact of the Bentayga eddy on the water column along the OceT, anomalies in σ_θ, Θ, and S_A were analyzed (Fig. 7). As noted earlier, it was surrounded by several cyclonic mesoscale eddies, which caused perturbations outside its horizontal boundaries, affecting the water column from stations 02–11 and 25–27 (Fig. 2d). To account for these external influences, the mean profiles used as a reference state for anomaly calculations were derived using Djurfeldt (1989) method. First, an average distribution was calculated as a function of σ_θ for depth, z, Θ, and S_A (i.e., $\overline{z}(\sigma_\theta)$, $\overline{\Theta}(\sigma_\theta)$, and $\overline{S_A}(\sigma_\theta)$). These averaged profiles were then interpolated back to the original z-coordinate and subtracted from the respective vertical sections.

https://doi.org/10.5194/egusphere-2025-99
Preprint. Discussion started: 28 January 2025

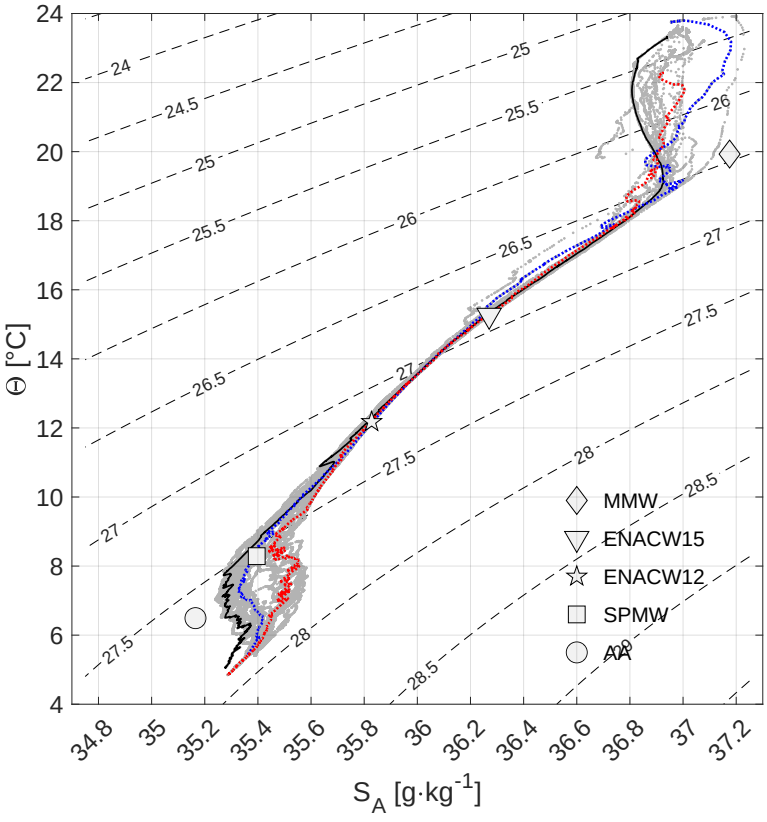

Figure 6. Conservative temperature (Θ) versus absolute salinity (S_A) distribution along the OceT transect, presented as a $\Theta - S_A$ diagram. Grey dots represent data from all oceanographic stations. The thermohaline structure at the eddy center (station 18) is highlighted with a thick black continuous line. Thermohaline properties from regions outside eddy's influence, westward (station 26) and eastward (station 04), are depicted with thick blue and red dashed lines, respectively. Symbols mark typical source water masses for the area (Alvarez et al., 2005), including Madeira Mode Water (MMW), Eastern North Atlantic Central Water (ENACW15 and ENACW12, at 15°C and 12°C, respectively), Subpolar Mode Water (SPMW), and diluted Antarctic Intermediate Water (AA). Thin black dashed lines denote σ_θ levels from 24 to 29 kg·m^{-3} at intervals of 0.5 kg·m^{-3}.

The anomalies associated with it were evident, with a core of lighter and warmer waters extending from the lower half of the core to approximately 500 m depth (<-0.2 kg·m^{-3} and >1°C, respectively), horizontally spanning stations 12–24 (Fig. 7a, b). The strongest anomalies in σ_θ and Θ were located at its base, near the σ_θ=25.5 kg·m^{-3} isopycnal (around -1 kg·m^{-3} and 4°C, respectively). Additionally, a fresher core was enclosed between the σ_θ=25.2 and 25.5 kg·m^{-3} isopycnals (with anomalies below -0.05 g·kg^{-1}). Below this layer, its presence induced saltier waters (anomalies >0.1 g·kg^{-1}) up to approximately 500 m depth (Fig. 7c).

https://doi.org/10.5194/egusphere-2025-99
Preprint. Discussion started: 28 January 2025

At intermediate depths (800–1300 m), colder and fresher anomalies corresponding to the higher presence of SPMW and AA (Fig. 6), <-0.25°C and <-0.1 g·kg^{-1}, respectively, were located just below the core of positive thermohaline anomalies (Fig. 7b, c).

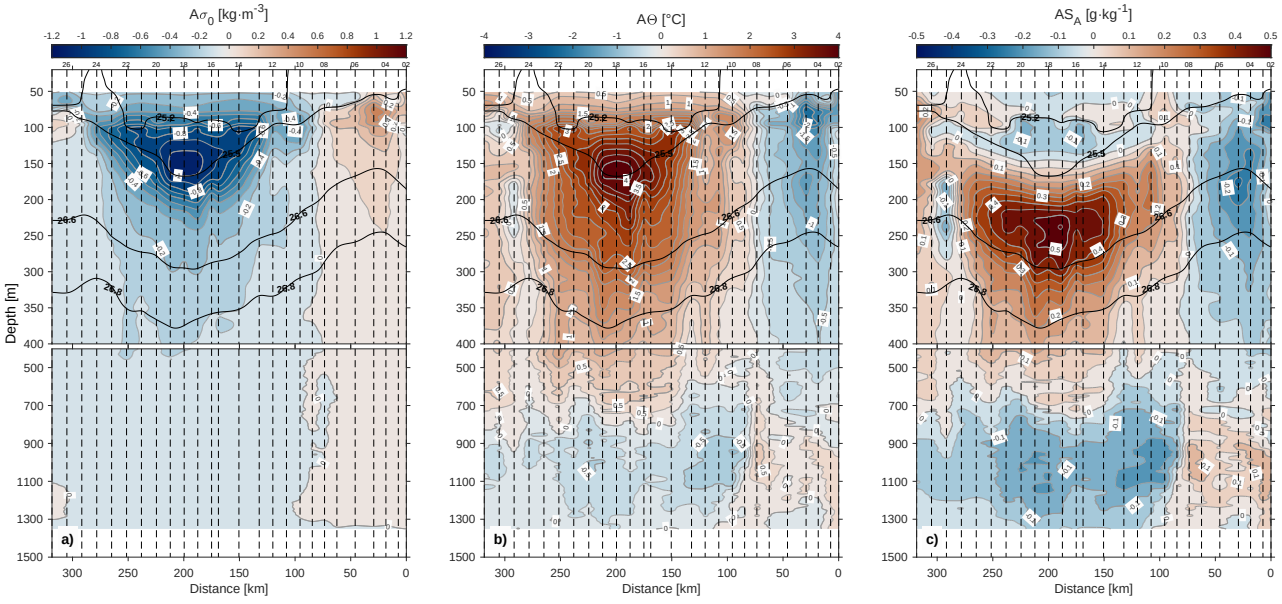

Figure 7. Vertical sections of anomalies in: a) potential density anomaly (Aσ_θ), b) conservative temperature (AΘ), and b) absolute salinity (AS_A) along the OceT transect during the eIMPACT2 survey. Thick black contours in all panels denote σ_θ levels at 25.2, 25.5, 26.6, and 26.8 kg·m^{-3}. Vertical dotted lines mark the positions of oceanographic stations, as illustrated in Fig. 4a. Consistent with Fig. 4, distinct vertical scales are used for the 0–400 m and 400–1500 m depth ranges.

3.3 3D view of the horizontal velocity field

The objectively interpolated fields of VMADCP velocity (*u, v*) and potential density anomaly (σ_θ) (Fig. 8) clearly reveal the dominant influence of the Bentayga eddy in the sampled area, with its anticyclonic circulation prevailing across much of the region and remaining evident even at the shallowest recorded depths (Fig. 8a). Outside this prominent circulation, the northwestern and southeastern corners of the interpolated field exhibited CEs with flow magnitudes comparable to those of this anticyclonic system. Additionally, a smaller AE was identified northeast of the primary system (Fig. 2d). This secondary structure, approximately half of its size, displayed weaker anticyclonic circulation. However, since it was located near the northeastern edge of the SeaSoar sampling grid, its geometry was likely underestimated.

Although the anticyclonic circulation of the Bentayga eddy was evident and coherent from approximately 40 m depth, the expected doming of the upper isopycnals around the core was subtle, consistent with observations along the OceT (Fig. 5). Horizontal sections in the upper 100 m (Fig. 8a, b) suggest that relatively lighter water was advected by the outer ring, circu-

https://doi.org/10.5194/egusphere-2025-99
Preprint. Discussion started: 28 January 2025

lating around the inner core. The presence of these lighter waters at the surface likely enhanced the vertical density contrast, potentially hindering or even preventing the rising of the upper isopycnals.

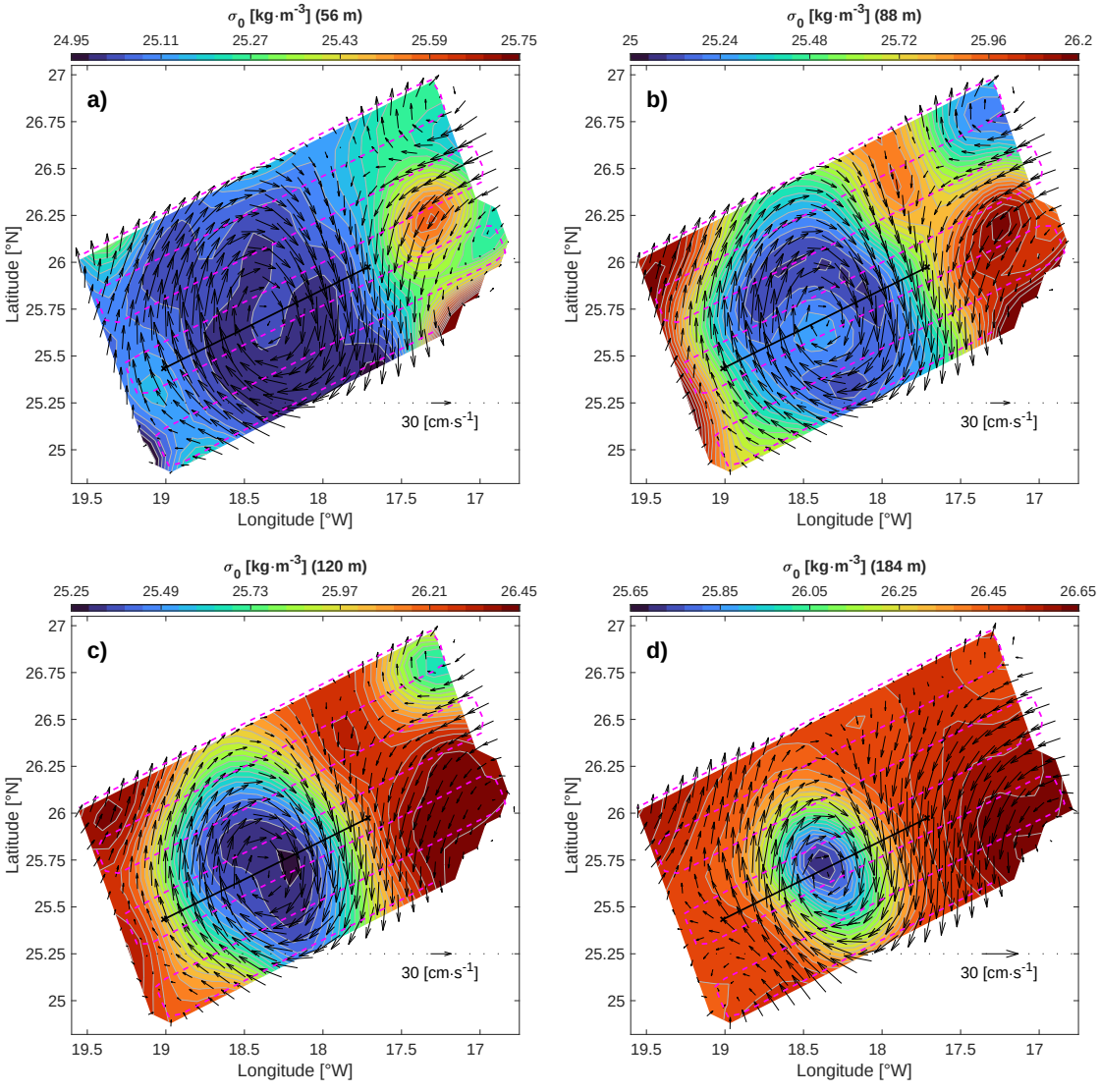

Figure 8. Objectively interpolated VMADCP velocity vectors (black arrows) superimposed on σ_θ contours at various depths: a) 56 m, b) 88 m, c) 120 m, and d) 184 m. Each panel displays a unique color scale and density range with 25 contour levels to highlight the isopycnal structure. Velocity vectors are scaled proportionally to the respective depth (see legend in the bottom right corner of each panel). The ship's grid-like sampling trajectory during the eIMPACT2 Seasoar phase (dashed magenta line) and the virtual transect used for the vertical section in Fig. 9 (solid black line) are also indicated. Objective interpolation correlation scales were set to $L_x = L_y = 44$ km, with 3% uncorrelated noise applied.

https://doi.org/10.5194/egusphere-2025-99
Preprint. Discussion started: 28 January 2025

At these depths, the eddy exhibited a generally circular, though slightly irregular, shape (horizontal aspect ratio of nearly 1.0), with meandering horizontal boundaries. As the depth increased, the structure became more regular and elliptical, maintaining a nearly constant horizontal aspect ratio of approximately 0.8 (Fig. 8c, d). The horizontal section at 120 m depth indicates that lighter water circulating around the inner core extended even at those depths (Fig. 8c).

These patterns may also be influenced by vertical circulation within ITEs, as reported in both simulations and observations (e.g. Barceló-Llull et al., 2017a; Estrada-Allis et al., 2019). Below 150 m, the Bentayga eddy was characterized primarily by local isopycnal deepening and exhibited a reduction in size with increasing depth (Fig. 8d).

In addition to the objectively interpolated fields of (u, v) and σ_0, the interpolated S_A field was also generated. Vertical sections were extracted along the virtual transect depicted in Fig. 8, offering a continuous depth-wise representation of the observed features and patterns (Fig. 9). The anticyclonic circulation associated with the studied ITE dominated the entire water column along this transect, with peak velocities exceeding 30 cm·s^{-1} in the upper 200 m (Fig. 9a). Within this vertical segment, just below the mixing layer, the isopycnals exhibited a steep inclination where the vertical density gradient was strongest.

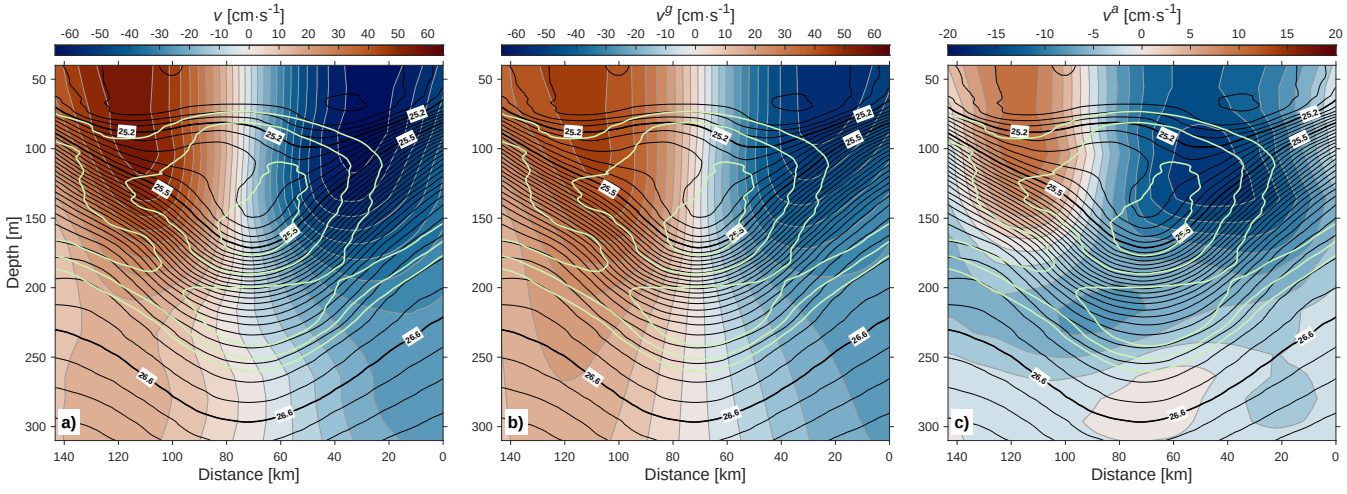

Figure 9. Objectively interpolated cross-transect velocity components along the virtual transect shown in Fig. 8. Panels represent: a) cross-transect velocities measured directly by the VMADCP (v), b) geostrophic velocities estimated using the thermal wind balance (v^g), and c) ageostrophic velocities calculated as the difference between VMADCP and geostrophic velocities ($v^a = v - v^g$). Black contours correspond to σ_θ levels (every 0.1 kg·m^{-3}), with thicker lines highlighting the 25.2, 25.5, and 26.6 kg·m^{-3} isopycnals, which are also labeled for reference. Light green contours denote isohalines (36.8–36.9 g·kg^{-1}, every 0.05 g·kg^{-1}).

The highest velocities (>50 cm·s^{-1}) were located at the eddy's edges, progressively converging towards the boundaries of the inner core with increasing depth. This subtle inward inclination was most pronounced between 80 and 150 m, where slight doming and deepening of the isopycnals delineating the inner core were also observed. Furthermore, within the inner core, the isopycnals displayed small-scale irregularities, characterized by doming on one side and deepening on the other side. These patterns were similarly reflected in the isohalines that defined the relatively less saline eddy core (36.8–36.9 g·kg^{-1}).

https://doi.org/10.5194/egusphere-2025-99
Preprint. Discussion started: 28 January 2025

The irregularities or perturbations in both isopycnals and isohalines align with the hypothesis of vertical isopycnal movement rather than the previously proposed horizontal advection of lighter water.

Using the thermal wind balance relationship, the geostrophic current field was derived from the interpolated density field, with VMADCP records at 312 m depth serving as the reference level (Fig. 9b). Generally, VMADCP-measured velocities were more intense than the geostrophic currents, though their spatial patterns showed only minor discrepancies. Similar to the VMADCP observations, geostrophic currents were strongest at depths shallower than 200 m (>30 cm·s^{-1}), with a gradual inward movement towards the inner core at greater depths. However, geostrophic velocities did not exceed ∼40 cm·s^{-1}, with maximum values observed above 100 m depth.

The ageostrophic secondary circulation was revealed by subtracting the geostrophic component from the VMADCP velocity field (Fig. 9c). These horizontal ageostrophic velocities were strongest within the upper 150 m of the water column (>5 cm·s^{-1}), peaking at over 10 cm·s^{-1} near the edges of the inner core, between 80 and 120 m depth.

3.4 Azimuthal velocity and angular dynamics

To investigate the dynamic features of the Bentayga eddy, the azimuthal velocity (u_θ) was analyzed across all recorded depth levels. As shown in panels a–c of Fig. 10, the eddy structure exhibited an inner core surrounded by distinct inner and outer rings, consistent with previous results. The width, rotation rate, and spatial coherence of these rings diminished with depth. A least squares fit of the polynomial $u_\theta = \omega_\theta \mathrm{r}$ to the $u_\theta(\mathrm{r})$ data at each depth was used to identify and characterize the solid-body rotation of the eddy's inner core. Here, ω_θ represents the angular velocity of the eddy, with the constraint $u_\theta = 0$ at the eddy center (r = 0). This fitting procedure also provided estimates of the effective radius and the depth range where this solid-body rotation persisted.

To refine these estimates, the fitting process was iteratively applied over varying radius lengths, and the effective radius was defined as the point where the correlation (r_{xy}) between the fit and the data reached its maximum. On average, the effective radius was approximately 25 km, aligning with the observed core length reported in Sect. 3.2. For depths where $r_{xy} \geq 0.9$, the solid-body rotation extended from the shallowest recorded level (∼40 m depth) to a depth of ∼350 m. Between 360 and 400 m, r_{xy} decreased to a minimum of ∼0.75. Interestingly, at greater depths, r_{xy} increased again, exceeding 0.9 between 415 and 450 m and remaining above 0.8 until 600 m, after which depth it sharply declined.

The depth variation of ω_θ, representing the rotation frequency, is shown in Fig. 10d. The frequency remained nearly constant down to 80 m, averaging approximately 1.35×10^{-5} rad·s^{-1} (corresponding to a ∼5-day period). It increased to a peak of 1.85×10^{-5} rad·s^{-1} (or a ∼3.9-day period) between 110 and 130 m. Below this depth, the rotation rate declined abruptly, dropping to approximately 70% of its peak value by 210 m, corresponding to a period of ∼11 days. This depth-dependent behavior suggests that the rotation of the inner core occurred in stratified layers, with each layer exhibiting distinct rotation rates rather than behaving as a uniform solid body. Such layered rotation in ITE cores has been observed in previous studies, including the kinetic and dynamic analysis of meddies by Schultz Tokos and Rossby (1991).

https://doi.org/10.5194/egusphere-2025-99
Preprint. Discussion started: 28 January 2025

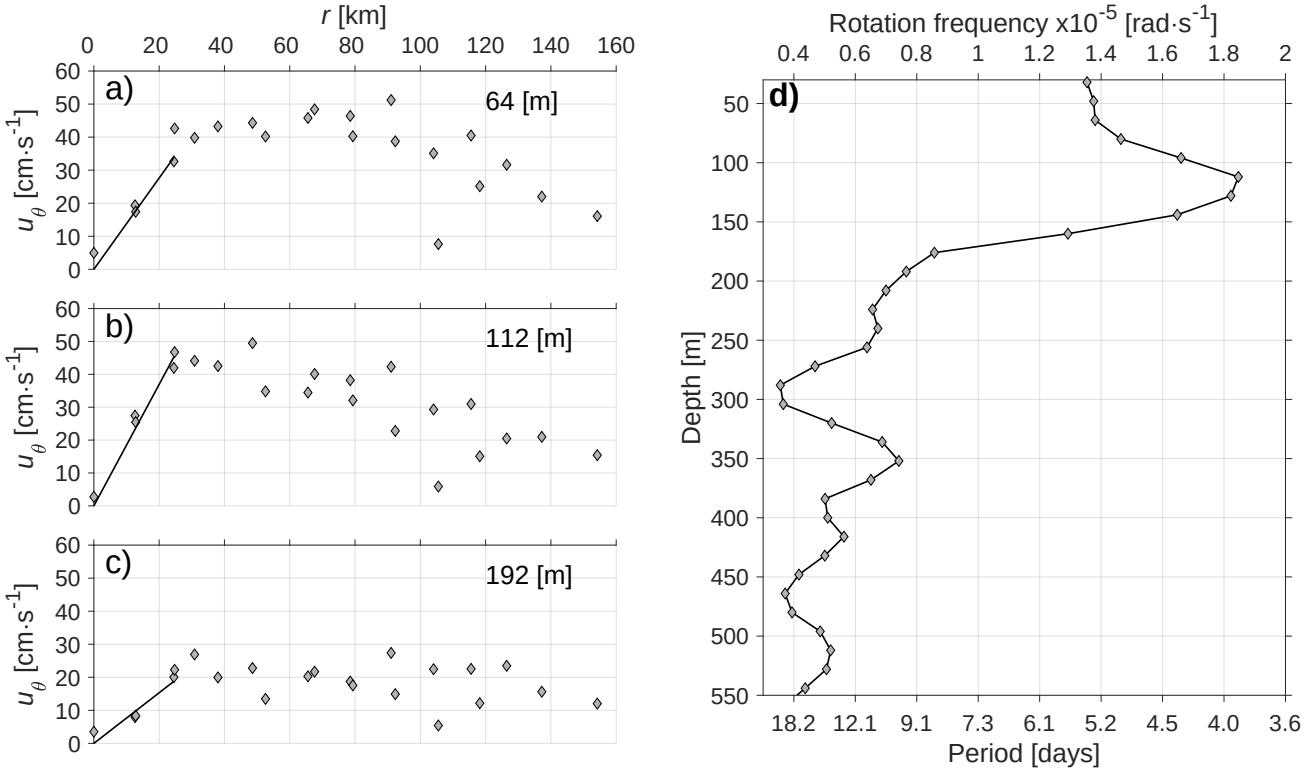

Figure 10. Radial profiles of azimuthal velocity (u_θ) for the OceT transect at selected depths: a) 64 m, b) 112 m, and c) 192 m, derived from the OceT. Grey diamonds represent the observed data, while solid black lines correspond to the linear regression fit using $u_\theta = \omega_\theta$r, with $u_\theta = 0$ at r = 0. The slope of the regression (ω_θ) is proportional to the angular velocity of the eddy. d) Depth-wise variation of the solid-body core's rotation frequency (ω_θ) and its corresponding period.

To dynamically characterize the internal structure of the Bentayga eddy, the Rossby number (Ro) was calculated as the ratio of the vertical component of the relative vorticity field to planetary vorticity (ζ and f, respectively). The relative vorticity (ζ) was derived from the interpolated VMADCP velocity fields using $\zeta = \partial v/\partial x - \partial u/\partial y$.

A horizontal section of the three-dimensional Ro field was extracted at a depth of 104 m, corresponding to the level of maximum VMADCP velocities recorded during the eIMPACT2 SeaSoar phase (Fig. 11a, see also Fig. 12). Additionally, a vertical section along the virtual transect shown in Fig. 11a was examined (Fig. 11b). These analyses revealed that its core was dominated by negative vorticity, with Ro values within the inner core reaching below -0.45 and a peak negative vorticity of approximately -0.61f at its center. Ro increased radially from the core toward the outer regions, transitioning to positive values in the outermost part of the inner ring, where Ro ranged between 0.1 and 0.2.

The horizontal location where the Ro sign changed was used to identify the position of the maximum circum-averaged velocities associated with the anticyclonic circulation induced by the Bentayga eddy. This boundary dynamically defined the

https://doi.org/10.5194/egusphere-2025-99
Preprint. Discussion started: 28 January 2025

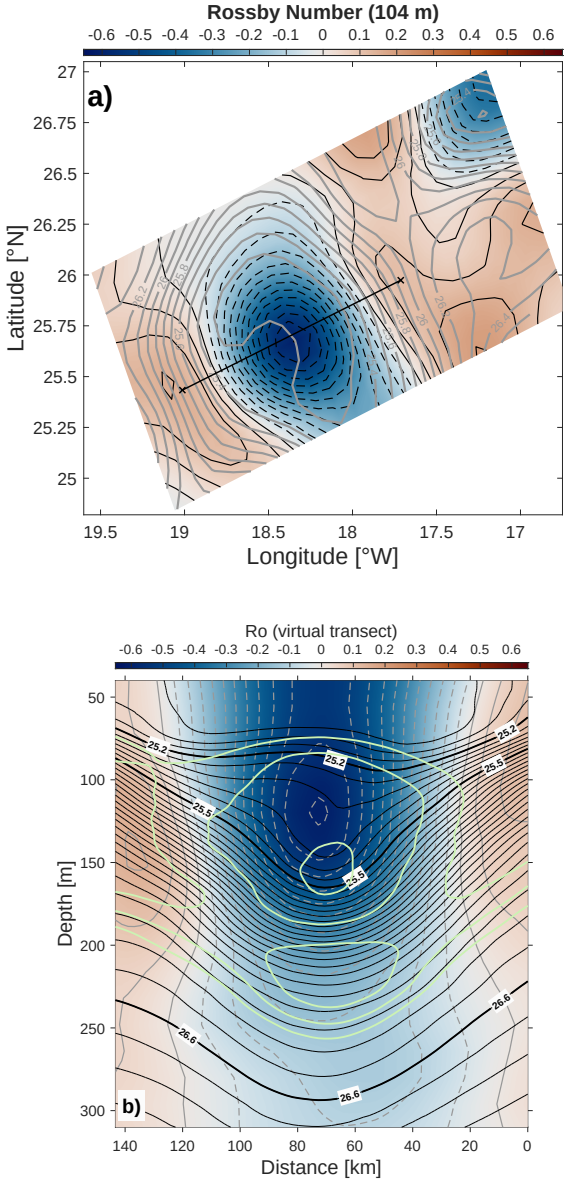

Figure 11. Rossby number (Ro) derived from the objectively interpolated VMADCP velocity fields. a) Horizontal section of Ro at 104 m depth, corresponding to the depth of maximum swirl speed of the eddy (refer to Fig. 12). Contours of Ro are shown every 0.05, with negative values represented by dashed lines and positive values by solid lines. b) Vertical section of Ro along the virtual transect in panel (a) (thick black line). Contours of Ro are displayed every 0.05, with dashed lines for negative values. Objectively interpolated σ_θ contours (every 0.1 kg·m^{-3}) are shown as grey and black lines, with σ_θ = 25.2, 25.5, and 26.6 kg·m^{-3} highlighted and labeled with thick black lines for clarity. Additionally, the 36.8–36.9 isohalines (every 0.05 g·kg^{-1}) are included as thick light green contours.

https://doi.org/10.5194/egusphere-2025-99
Preprint. Discussion started: 28 January 2025

external (internal) edge of the inner (outer) ring, with an average radius of 65 km. These velocities delineated the shell enclosing the internal region of the eddy, which included the inner ring and solid-body core, contributing to its non-linearity, i.e., its ability to trap water within. The position of these shell velocities was determined at each depth, and their vertical profile, along with the corresponding standard deviation, is presented in Fig. 12.

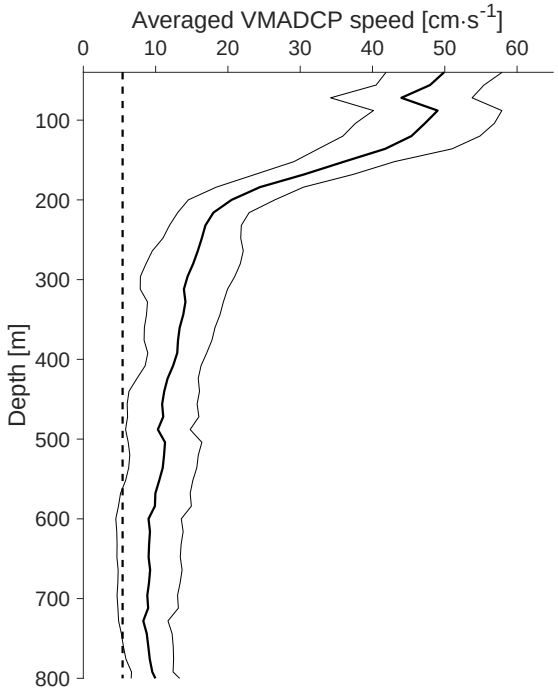

Figure 12. Vertical profile of the horizontally averaged maximum VMADCP velocity (thick black line) with the corresponding standard deviation represented by thin black lines. The dashed vertical line indicates the average translational speed of the eddy (5.4 cm·s^{-1}) during the eIMPACT2 survey.

Maximum shell velocities were observed near the surface, at depths shallower than 120 m, with a relative peak centered at 104 m (approximately 50 ± 10 cm·s^{-1}). Below this peak, the shell velocity magnitude decreased sharply, extending down to 200 m depth, with a mean vertical shear of 0.004 s^{-1}. At greater depths, the velocity reduction was more gradual, with a mean shear of 0.002 s^{-1} down to about 600 m depth. As shown in Fig. 10a, beginning at 550 m depth, the velocity magnitudes approached mean translation velocity (c) of the Bentayga eddy. Between 550 and 750 m depth, the velocities even dropped below this translation speed, suggesting that at these depths the eddy's water trapping capacity may no longer be sufficient to significantly limit exchange with the surroundings, thereby reducing its ability to transport and maintain these water masses along its trajectory.

https://doi.org/10.5194/egusphere-2025-99
Preprint. Discussion started: 28 January 2025

3.5 Potential vorticity and stratification

The radial distribution of Ro provides insight into the eddy's rotational dynamics and helps delineate its core structure and boundary layers. Complementary to this, the vertical stratification and PV fields highlight the internal water column stability and the extent of PV anomalies within the eddy. These analyses together elucidate the interplay between the eddy's rotational dynamics and its stratification-driven trapping capacity.

As discussed earlier (Section 2.3.1), ITEs are characterized by extremely low-PV values within their core, primarily due to the homogeneous water they enclose, resulting in significant negative PV anomalies relative to the surrounding environment. The calculated PV of the Bentayga eddy related to isopycnal tilting was found to be two orders of magnitude smaller than the PV associated with water column stretching. This aligns with previous findings, such as those for the PUMP eddy by Barceló-Llull et al. (2017a), and reflects the general expectation for ITEs, where the vertical density gradient, $\partial_z \sigma_\theta$, i.e., the stratification of the water column, predominantly controls the magnitude of PV.

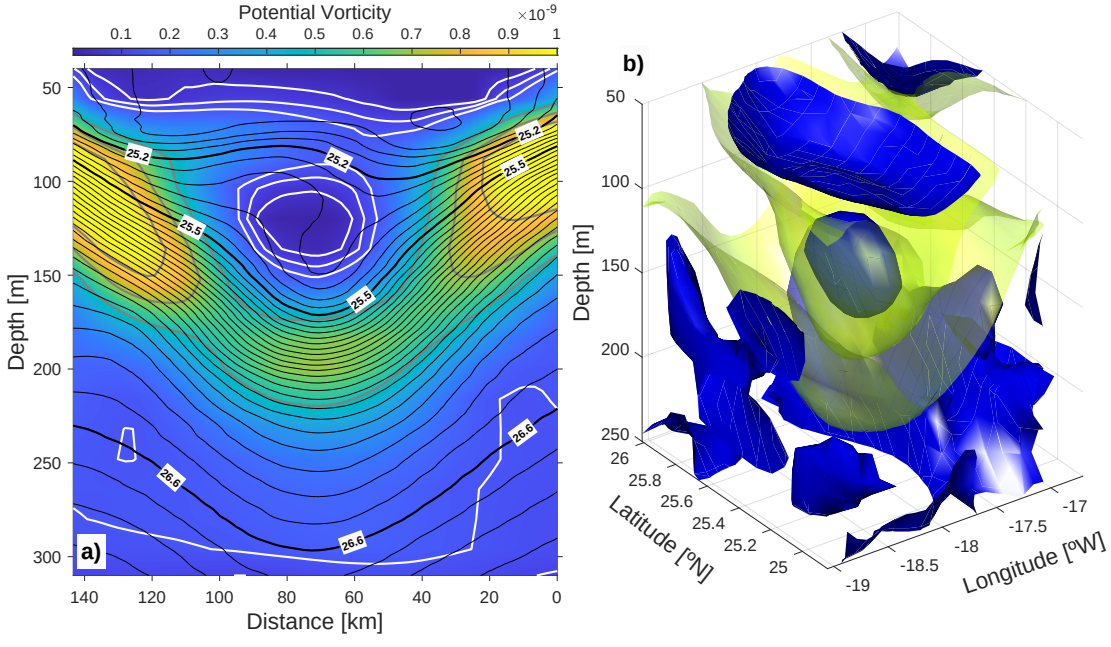

Figure 13. Ertel's potential vorticity (PV) derived from objectively interpolated VMADCP velocities and σ_θ fields. a) Vertical section of PV along the virtual transect indicated by the thick black line in Figs. 8 and 11a. Extreme PV levels are represented by thick white and grey contours, highlighting the lowest (5×10^{-11}, 10×10^{-11}, and 15×10^{-11} $m^{-1} \cdot s^{-1}$) and highest PV values (5×10^{-10}, 7×10^{-10}, and 9×10^{-10} $m^{-1} \cdot s^{-1}$), respectively. Thin black contours indicate σ_θ levels (spaced every 0.1 kg·m^{-3}). For clarity, σ_θ levels at 25.2, 25.5, and 26.6 kg·m^{-3} are labeled and displayed as thick black lines. b) Three-dimensional view of the PV field, represented by the 15×10^{-11} and 5×10^{-10} $m^{-1} \cdot s^{-1}$ surfaces, shown as dark blue and light yellow sheet-like patches, respectively.

https://doi.org/10.5194/egusphere-2025-99
Preprint. Discussion started: 28 January 2025

As seen in Fig. 13, the lowest PV values ($\sim 10^{-11}$ m$^{-1} \cdot$ s^{-1}) were observed in the shallowest layers and within the inner core, where water exhibited high homogeneity and low stratification. As anticipated, higher PV values ($> 5 \times 10^{-10}$ m$^{-1} \cdot$s^{-1}) were detected in regions of greater stratification, where closely spaced isopycnal surfaces indicated compression of the water column in the vertical dimension. The highest PV values ($> 9 \times 10^{-10}$ m$^{-1} \cdot$s^{-1}) were associated with isopycnal lifting induced by CEs adjacent to the Bentayga eddy.

Furthermore, the spatial distribution of PV highlights the sharp stratification contrast between its extremely low-PV core and the surrounding layers of relatively higher PV (Fig. 13b). At greater depths, below these surrounding layers, PV values diminished gradually, reaching approximately 1×10^{-10} m$^{-1} \cdot$ s^{-1}, indicating a progressive decrease in PV distribution with depth.

3.6 Energy content

The net APE and KE within the Bentayga eddy were estimated using Eq. 2 and Eq. 3, integrating from the eddy center to the external radius of its inner ring (R = 65 km) and from its effective trapping depth (H = 550 m) to the surface (Table 1). During the eIMPACT2 survey, the APE was 33% higher than the KE, with values of 0.027 PJ and 0.018 PJ, respectively.

This predominance of APE over KE is a hallmark of well-established ITEs and consistent with findings from previous studies (e.g., Schultz Tokos and Rossby, 1991; Schmid et al., 1995; Fernández-Castro et al., 2020). In addition, it reflects a specific stage in the ITE life cycle during which the balance between these two forms of energy evolves (e.g., Schultz Tokos and Rossby, 1991). In contrast, the PUMP eddy, also sampled within the CEC, exhibited a KE value 50 % higher than its APE (Barceló-Llull et al., 2017b). This divergence is notable given that both eddies were of similar age at the time of their respective surveys, suggesting potential differences in their formation mechanisms, environmental interactions, or life cycle stages.

The ratio between the two types of energy defines the energy Burger number (B_E = KE/APE), which for the Bentayga eddy was calculated to be 0.68. To explore the factors contributing to this B_E, it was analyzed in terms of the length-scale Burger number ($B_L = N^2 L_Z^2 / f^2 L_X^2$) and the Ro, using the relationship ${B_E}^L \approx B_L/(1+Ro)^2$ (Prater and Sanford, 1994). B_L was determined using a background stratification value (N^2) of 3.6×10^{-5}s^{-2}, a Coriolis parameter (f) of 6.32×10^{-5}s^{-1}, and the characteristic horizontal diameter (L_X = 2R = 130 km) and vertical extent (L_Z = H = 550 m) of the Bentayga eddy. This yielded a representative B_L of 0.16. With a Ro of -0.47, representative of the inner core conditions, a ${B_E}^L$ value of 0.57 was obtained.

Although minor discrepancies exist between these B_E estimates, the results suggest that its energy content is primarily influenced by its geometry (aspect ratio $H/L_X = 0.42\%$) and the strong negative vorticity within its interior. Previous studies (e.g., McWilliams, 1985; Chelton et al., 2011) emphasized the importance of aspect ratio in controlling eddy energetics, while Schultz Tokos and Rossby (1991) highlighted the role of strong vorticity in shaping the kinetic and potential energy distribution within mesoscale ocean structures.

https://doi.org/10.5194/egusphere-2025-99
Preprint. Discussion started: 28 January 2025

Table 1. Comparison of energy content in ITEs. The vertical extent (H) and characteristic radius (R) used to calculate ITE's available potential energy (APE) and kinetic energy (KE) are listed alongside their resulting energy values and energy Burger number (B_E = KE/APE). Additionally, the length-scale Burger number ($B_L = N^2 {L_Z}^2 / f^2 {L_X}^2$), Rossby number, and the inferred energy Burger number ($B_E{}^L = B_L/(1+Ro)^2$) are presented. Here, the background Brunt-Väisälä frequency (N), the coriolis parameter (f), and the eddy's vertical and horizontal scales (L_Z and L_X, respectively), used for the calculations are also included. When L_Z and L_X correspond to the spatial domain used for APE and KE calculations, the associated values of H and R, as defined in this table, are referenced.

ITE's properties	Bentayga	Schultz Tokos and Rossby (1991): Meddy (October 1984)	Schultz Tokos and Rossby (1991): Meddy (October 1985)	Prater and Sanford (1994): A two core newly formed Meddy	Schmid et al. (1995): AE *Vitória* Brazil Current	Barceló-Llull et al. (2017b): PUMP	Fernández-Castro et al. (2020): AE west off Great Abaco Island
H (m)	550	900	600	650	400	500	1000
R (km)	65	65	40	9	50	46	80
APE (x10^{13} J)	26.8	7.5	2.1	0.2	19.0	5.6	438
KE (x10^{13} J)	18.1	7.9	1.2	0.4	9.6	8.9	36
B_E	0.68	1.05	0.57	2.00	0.51	1.59	0.08
N^2 (x$10^{-5}s^{-1}$)	3.6	-	-	0.8	-	2.8*	2.5
f (x$10^{-5}s^{-1}$)	6.3	7.7	6.6	8.6*	5.1*	6.4*	7.1*
L_Z (m)	H	-	-	H	-	H	500
L_X (km)	2R	-	-	2R	-	2R	120
B_L	0.2	-	-	1.4	-	0.2	0.1*
Ro	-0.5	-0.3	-0.4	-0.9	-0.2	-0.6	-0.1
$B_E{}^L$	0.57	-	-	61.54*	-	1.25	0.09

The * symbol denotes values that were not explicitly provided in the respective studies.
These were inferred from figures, calculated using related information, or estimated based on the provided methodology.
Assumptions and approximations for these values are detailed in their respective references.

https://doi.org/10.5194/egusphere-2025-99
Preprint. Discussion started: 28 January 2025

3.7 Thermohaline anomalies and transport

Distinct thermohaline anomalies were identified within the Bentayga eddy compared to the surrounding environment (Fig. 7). These anomalies served as the basis for calculating the Available Heat Anomalies (AHA) and Available Salt Anomalies (ASA). Radial integration from the eddy center to the outer boundary of the inner core ($R_c = 25$ km) revealed pronounced vertical deviations between the distributions of ASA(z) and AHA(z) (Fig. 14).

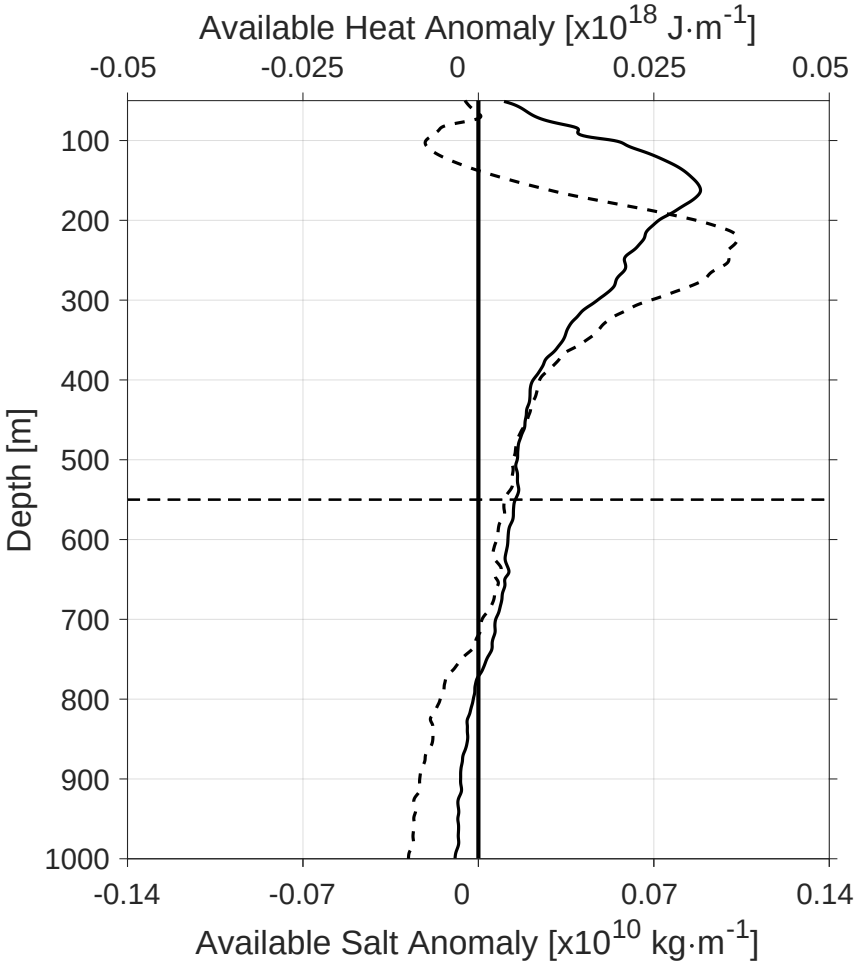

Figure 14. Vertical profiles of radially integrated available heat anomaly (AHA(z)) and available salt anomaly (ASA(z)) within the inner core of the eddy (R_c = 25 km). The solid black line represents AHA(z), while the dashed black line corresponds to ASA(z). The horizontal dashed line indicates the effective trapping depth (H = 550 m), serving as the lower limit for vertical integration.

ASA(z) displayed predominantly positive values, except within the vertical range of 0–150 m and below 700 m. Shallow negative anomalies, attributed to the salinity deficit in its inner core, reached a minimum of -0.20 Gkg·m^{-1} at 112 m depth.

https://doi.org/10.5194/egusphere-2025-99
Preprint. Discussion started: 28 January 2025

Below this point, ASA(z) steadily increased, peaking at 0.96 Gkg·m^{-1} at 231 m, before declining at a rate of 3.0 Mkg·m^{-2} down to 400 m. Beyond this depth, the decrease continued more gradually, averaging 0.8 Mkg·m^{-2}.

In contrast, AHA(z) remained consistently positive from the uppermost studied layer (∼50 m) to 750 m depth. Its maximum value of 29.0 PJ·m^{-1} occurred at 160 m, notably shallower than the ASA(z) peak. While AHA(z) exhibited no negative values, a relative reduction in magnitude at 90 m briefly interrupted the general increasing trend leading to the maximum. This growth followed a rate of -0.3 PJ·m^{-2}. Below 160 m, AHA(z) declined at 0.1 PJ·m^{-2} until 400 m, transitioning to a more gradual decrease of 0.02 PJ·m^{-2} at greater depths.

Given that the critical trapping depth of the Bentayga eddy was 550 m, the negative anomalies in ASA(z) and AHA(z) below 700 m were unlikely to be influenced by the eddy. Vertical integration of ASA(z) and AHA(z) to the trapping depth yielded total values of 0.016 Tkg and 7.052 EJ, respectively. These positive totals underscore the persistence and intensity of heat and salt anomalies, despite localized negative segments in ASA(z).

During the eIMPACT2 campaign, the Bentayga eddy followed a west/southwest trajectory at an average speed of 4.7 km·day^{-1}, aligning with the propagation speed of nondispersive baroclinic Rossby waves (Chelton et al., 2007). Using this translational speed (c), along with its geometric dimensions ($R_c = 25$ km and H= 550 m), the eddy-driven V_e was estimated at 1.47 Sv. This value closely matches the flux of the PUMP eddy (1.38 Sv), calculated using Eq.(6) and the parameters reported by Barceló-Llull et al. (2017a), and aligns with the mean transported volume of 1.3 Sv in the CEC estimated by Sangrà et al. (2009). When compared to other EBUS, the eddy-driven volume fluxes observed in this region exceed the average values reported for the Peru-Chile Current System (PCCS) (Chaigneau et al., 2011; Hormazabal et al., 2013) but remain lower than those observed in the Eastern Indian Ocean (Dilmahamod et al., 2018).

In terms of heat transport, the Bentayga eddy generated an Q_{eh} of 5.13 TW, an order of magnitude higher than averages reported in the PCCS (Chaigneau et al., 2011) and the Western and Eastern Indian Ocean (Dilmahamod et al., 2018). The eddy also contributed to a Q_{es} of 0.47 Gkg·s^{-1} and a Q_{fw} of -0.013 Sv. These values are consistent with those reported for the PCCS (Chaigneau et al., 2011), assuming similar upper-ocean conditions (see Sect. 3.7 and Eq.(9)), and are an order of magnitude lower than averages observed in the Indian Ocean (Dilmahamod et al., 2018).

4 Discussion

The CEC is renowned for its intense eddy activity and elevated levels of Eddy Kinetic Energy (EKE) (Barton et al., 1998; Sangrà et al., 2009). This high EKE primarily results from the interaction of the CC with wind-driven upwelling and the orographic influence of the Canary Islands, generating mesoscale eddies that propagate westward into the open ocean (La Violette, 1974; Van Camp et al., 1991; Hernández-Guerra et al., 1993; Arístegui et al., 1994, 1997; Barton et al., 2000; Basterretxea et al., 2002; Pelegrí et al., 2005). Among these features, ITEs are long-lived mesoscale structures that persist for several months and play a critical role in maintaining the region's elevated EKE. The dense population of eddies in the CEC further promotes frequent eddy-to-eddy interactions (Sangrà et al., 2005).

https://doi.org/10.5194/egusphere-2025-99
Preprint. Discussion started: 28 January 2025

Despite their significance, detailed hydrographic and dynamic studies of ITEs within the upper 500 m of the water column in the CEC are scarce. Prior to this study, only one ITE, the PUMP eddy (Barceló-Llull et al., 2017b), had been comprehensively analyzed. Formed south of Tenerife Island and studied during its mature phase, this ITE exhibited dual cores: a shallow one at 80–100 m depth with azimuthal velocities exceeding 30 cm·s^{-1}, and a deeper core at 250 m depth containing Madeira Mode Water (MMW). By September 2014, it had traveled approximately 550 km southwestward over a period of nearly four months.

In contrast, the Bentayga eddy, as examined in this study, displayed a single cohesive core spanning 80–220 m depth, with maximum azimuthal velocities exceeding 40 cm·s^{-1} and relatively homogeneous salinities between 36.8 and 36.95 g·kg^{-1}. These differences reflect variations in the physical processes and environmental conditions experienced by the eddies between formation and sampling.

The hydrographic properties of its inner core suggest significant trapping of upwelling waters from filaments near Cape Juby and Cape Bojador during its intensification in August 2022 (Fig. 15). Satellite images of chlorophyll-a concentration and sea surface temperature from this period reveal upwelling filaments spiraling toward the eddy's center, indicating surface convergence consistent with theoretical models of anticyclonic eddy growth (Sangrà et al., 2005, 2007). By contrast, the PUMP eddy showed no evidence of interactions with upwelling waters along its trajectory (see Fig. 1 in Barceló-Llull et al., 2017b).

Interactions between mesoscale eddies, a common feature in the CEC, can modify hydrographic properties within their cores and occasionally result in structural merging (Sangrà et al., 2005; Rodríguez-Marroyo et al., 2011; Ruiz et al., 2014). Such processes likely contributed to the variability observed in the Bentayga eddy, distinguishing it from PUMP and emphasizing the complexity of mesoscale dynamics in the region.

The Bentayga eddy displayed a well-defined anticyclonic circulation from the shallowest VMADCP-recorded level (40 m depth) to approximately 230 m. Below this depth, horizontal sections of the interpolated velocity field during the eIMPACT2 SeaSoar phase (Figs. B1 and B2) indicated a northward displacement of the circulation center between 250 and 380 m. At 320 m, the core appeared elongated, possibly representing a center with two nuclei, though this may also reflect artifacts of the interpolation technique. Between 380 and 420 m, the anticyclonic circulation weakened but retained spatial coherence. At greater depths, coherence became increasingly irregular; while anticyclonic features persisted, they were no longer dominant.

This behavior suggests that the direct anticyclonic influence of this ITE may be limited to shallower depths, potentially constrained by the maximum depth where the correlation (r_{xy}) between azimuthal velocity observations (u_θ) and the least squares polynomial fit ($u_\theta = \omega_\theta r$) exceeded 0.9, prior to the first local minimum (H_{max} = 350 m, see Sect. 3.4). Below this depth, the observed circulation could instead reflect the lifting of isopycnals induced by neighboring CEs. If so, the analyses may have misinterpreted these dynamics due to challenges in fully isolating external contributions from the intrinsic processes of this ITE.

Furthermore, previous studies in the CEC have documented the trapping of near-inertial waves at the base of ITEs (Martínez-Marrero et al., 2019), which may dominate current variability beyond a critical depth. Additionally, its proximity to the Canary Archipelago, nearby seamounts, and the continental slope and shelf of the northwestern African coast (Fig. 1) could expose the eddy to internal waves with super-inertial frequencies (e.g., semidiurnal internal tides), potentially modulating circulation and hydrographic variability.

https://doi.org/10.5194/egusphere-2025-99
Preprint. Discussion started: 28 January 2025

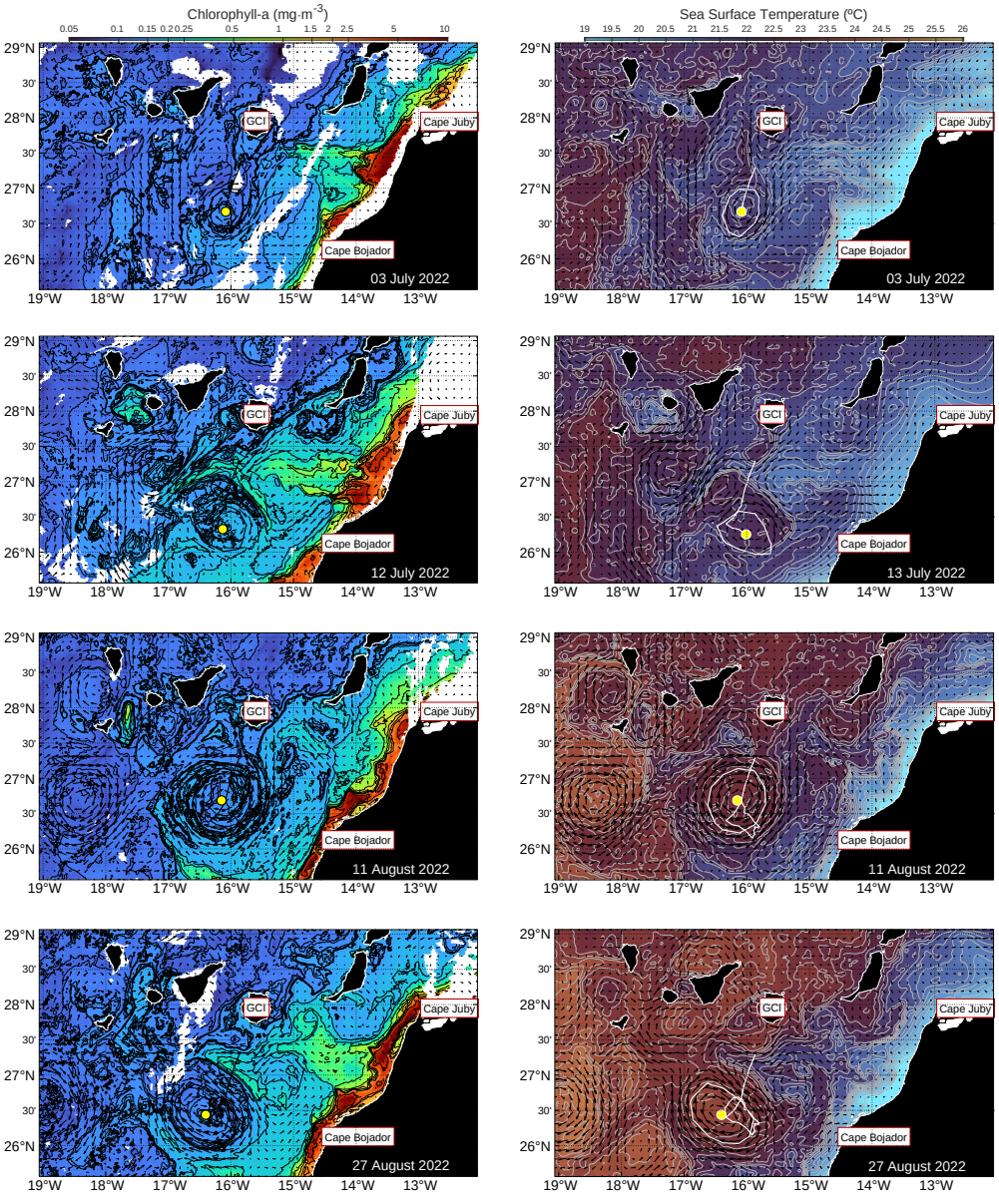

Figure 15. Interaction between coastal upwelling filaments and the mesoscale eddy. Left panels depict chlorophyll-a concentration, while right panels display sea surface temperature, both overlaid with geostrophic currents derived from satellite altimetry (black arrows). Snapshots correspond to key dates during the eddy's intensification phase, illustrating its interaction with upwelling filaments along the NW African coastal margin. The thick black (left panels) and white (right panels) lines represent the eddy's trajectory, with its position at each date marked by a yellow circle. Note the spiraling of upwelling filaments toward the eddy's center, consistent with the surface convergence dynamics described in Sect. 4.

https://doi.org/10.5194/egusphere-2025-99
Preprint. Discussion started: 28 January 2025

These complexities highlight the importance of employing advanced interpolation techniques to accurately extract and characterize the true signal of the eddy from the observed current and hydrographic data. Addressing these limitations and separating external influences would require a more detailed analysis, which is beyond the scope of this study (e.g., Candela et al., 1992).

The geometry of the Bentayga eddy aligns with the typical characteristics of AEs in the Macaronesian region (Table 2). However, given its radius and vertical extent, this ITE ranks within the upper 20 percent, classifying as a relatively large AE (Table 2). This classification is further supported by its $B_E < 1$, which is calculated as the ratio of KE to APE and indicative of large mesoscale vortices (Table 1).

Its elevated KE content—more than double that of the PUMP eddy (Barceló-Llull et al., 2017b) and certain meddies in the northeastern Atlantic (Schultz Tokos and Rossby, 1991; Prater and Sanford, 1994)—can be attributed to its larger outer radius, approximately 20 km greater than that of the PUMP eddy, and its position in the upper water column, where horizontal density gradients are more pronounced. Moreover, its KE was comparable to that of the most energetic eddies observed along western ocean basin boundaries. For instance, as shown in Table 1, Bentayga's KE was half that of a large anticyclonic mode-water eddy in the western North Atlantic (Fernández-Castro et al., 2020), and nearly double that of a surface AE in the South Atlantic (Schmid et al., 1995).

The core of the Bentayga eddy exhibited positive temperature and salinity anomalies, except within the 80–120 m depth range, where negative salinity anomalies were observed. These anomalies slightly exceeded those previously reported for AEs in this region (Table 2). However, rather than being associated with a distinct water mass, they reflect the typical characteristics of the Eastern North Atlantic Central Water (ENACW). This contrasts with the PUMP eddy, whose core contained MMW (Barceló-Llull et al., 2017b, see Table 2), and subsurface ITEs formed near Mauritania's coast, which may transport South Atlantic Central Water (SACW) into open ocean waters enriched with North Atlantic Central Water (NACW) (Schütte et al., 2016; Karstensen et al., 2017, see Table 2).

The volume, heat, and salt (or freshwater) fluxes generated by the Bentayga eddy during the eIMPACT2 survey align with previously reported values for AEs in the CEC (Sangrà et al., 2009; Barceló-Llull et al., 2017b), as well as in other EBUS (Chaigneau et al., 2011; Dilmahamod et al., 2018) and western boundary current regions (Dilmahamod et al., 2018). However, as an ITE, Bentayga is distinct due to its subsurface intensification and its capacity to trap and transport water masses at thermocline depths. These characteristics position ITEs as efficient vectors for delivering thermal and saline anomalies to the ocean interior, in contrast to surface-intensified eddies (Dilmahamod et al., 2018).

Interactions with upwelling filaments extending from the northwestern African coast (Fig. 15) likely imbued the Bentayga eddy with heat and salt signatures characteristic of these features. As it migrated into the open ocean, these waters may have undergone subduction (e.g., Pingree, 1996), driven by radial convergence, isopycnal adjustment, and potential vorticity conservation. In this context, this ITE acted as a conduit, transporting coastal upwelling waters and their associated properties into the ocean interior.

Table 2. General properties of previously studied anticyclonic eddies (AEs) in the Macaronesian region. The Table summarizes key characteristics of AEs reported in various studies, including the eddy type, study location, radius (R), vertical extent (H), vertical aspect ratio (H/L_X), temperature anomaly ($A\Theta$), salinity anomaly (AS_A), vertical displacement of a characteristic isopleth (h'), water mass types in the AE core (WM), and Rossby number ($Ro = \zeta/f$). For ensemble averages, properties represent statistical means, whereas for individual AEs, the specific values are provided. Where applicable, vertical displacement (h') values are listed without parentheses for sinking isopleths, while values in parentheses represent shoaling isopleths. Mean, standard deviation, mode, median, and 80th percentile values for all listed studies are included, along with Bentayga's for comparison. See the respective references for additional details on study-specific methods and results.

Study (authors)	AE type	Location	R (km)	H (m)	H/L_X	$A\Theta$ (°C)	AS_A (g·kg^{-1})	h'(m)	WM	Ro
Armi and Zenk (1984)	Subsurface eddy from in situ observations	Canary Basin	50.0	900	0.0090	2.50	0.800	-	MW	-
Arístegui et al. (1994)	Surface eddy from in situ observations	Lee of Canary Archipelago	31.0	400	0.0065	1.00	-	45	-	-
Pingree (1996)	Subsurface eddy from in situ observations	Northeastern Atlantic Ocean	42.0	300	0.0014	1.40	0.350	80 (40)	-	-0.3
Sangrà et al. (2009)	Eddy Demography based on satellite altimetry	Canary Eddy Corridor	50.0	300	0.0030	-	-	-	-	-
Caldeira et al. (2014)	Surface eddy from satellite and in situ observations	Lee of Madeira Island	25.0	300	0.0060	-	-	100	-	-0.7
Ruiz et al. (2014)	Surface eddy from satellite and in situ observations	Off Cape Bojador	62.5	250	0.0020	0.80	0.200	40	ENACW	-
Pegliasco et al. (2015)	Ensemble mean eddy based on satellite altimetry and Argo observations	Canary Upwelling System	52.0	325	0.0034	0.60	0.120	-	-	-
Schütte et al. (2016)	Ensemble mean subsurface eddy based on satellite altimetry and Argo observations	Tropical northeastern Atlantic	52.0	325	0.0034	-4.00	0.720	52 (48)	SACW	-
Karstensen et al. (2017)	Subsurface eddy from in situ observations	Tropical northeastern Atlantic	30.0	200	0.0033	-2.00	-0.600	50 (20)	SACW	-0.7
Barceló-Llull et al. (2017b)	Subsurface eddy from in situ observations	Canary Eddy Corridor	46.0	500	0.0054	1.50	0.300	150 (40)	MMW	-0.6
Kolodziejczyk et al. (2018)	Subsurface eddy from in situ observations	Off Cap-Vert Peninsula	100.0	600	0.0030	-	-	40 (40)	SACW (NACW)	-
Estrada-Allis et al. (2019)	Surface eddy from a regional simulation	Canary Eddy Corridor	40.9	800	0.0098	-	-	45	-	-0.7
Cardoso et al. (2020)	Eddy demography based on satellite atimetry	Cabo Verde	50.0	-	-	-	-	-	-	-
Ioannou et al. (2022)	Eddy demography based on satellite atimetry and Argo observations	Northern Canary Current Upwelling System	56.6	120	0.0011	0.45	0.140	-	-	-
Dilmahamod et al. (2022)	Subsurface eddy from a regional simulation	Mauritanian Upwelling region	31.6	300	0.0047	-4.50	-0.800	40 (50)	SACW	-0.7
		Mean	53.8	414	0.0043					-0.6
		Standard deviation	29.9	182	0.0025					0.2
		Mode	50.0	300	0.0030					-0.7
		Median	48.0	300	0.0033					-0.7
		80th percentile	62.5	520	0.0064					-0.7
		Bentayga	65.0	550	0.0042	1-4	>0.1	75 (10)	ENACW	-0.5

https://doi.org/10.5194/egusphere-2025-99
Preprint. Discussion started: 28 January 2025

Beyond their physical transport of heat and salt, ITEs such as the Bentayga eddy play a pivotal role in biogeochemical exchanges by potentially delivering nutrient-rich upwelling waters to oligotrophic regions. These processes can stimulate offshore primary productivity, highlighting the ecological importance of ITEs in shaping regional ocean dynamics (e.g., Hormazabal et al., 2013; Thomsen et al., 2016; Cornejo D'Ottone et al., 2016; Karstensen et al., 2017; Bosse et al., 2017; Cerdán-García et al., 2024).

Extrapolating observed fluxes to estimate annual eddy-driven transport is a common practice once the average frequency of eddy formation in a region is established. For instance, using satellite altimetry and previous estimates, Sangrà et al. (2009) calculated an annual volume transport of 1.3 Sv by long-lived eddies in the CEC, representing approximately one-quarter of the Canary Current's total annual transport, based on an average of 17 eddies per year. However, the capacity of eddies to transport heat, salt, and biogeochemical properties can vary widely depending on their lifespan, size, intensity, and interactions with surrounding waters.

Applying transport values from the Bentayga eddy to the broader context of the CEC presents certain challenges. Nevertheless, its distinct trajectory and unique characteristics underscore its significant contribution to understanding eddy variability in the region. An analysis of the climatological eddy detection atlas (META3.2 DT *allsat*; Aviso+, 2022), spanning 1993–2022, identified only six AEs with trajectories resembling Bentayga's, each remaining near the continental shelf for over 10 days. This rare behavior positions this ITE as a valuable case for investigating eddy-driven transport, offering insights into the dynamics that facilitate the movement of coastal upwelling waters into the ocean interior.

During the eIMPACT2 campaign, the Bentayga eddy was flanked by two cyclonic eddies (CEs). A visual inspection of satellite altimetry images along its trajectory (not shown) revealed the persistent presence of multiple mesoscale vortices, including both CEs and AEs, in its vicinity. It is plausible that the six identified AEs may have undergone similar interactions with neighboring eddies within the CEC.

Eddy-to-eddy interactions play a crucial role in influencing the transport of water masses originating from coastal regions. These interactions, whether through merging or straining, can enhance mixing and facilitate water mass exchanges (de Marez et al., 2020; Rykova and Oke, 2022; Fu et al., 2023). Consequently, such processes increase the likelihood of coastal water masses penetrating deeper into the ocean interior, thereby amplifying the transport potential of eddies like Bentayga.

The findings presented in this study offer a comprehensive understanding of the physical characteristics (e.g., hydrography and dynamical properties) of the Bentayga eddy and its role within the CEC as an ITE. This eddy demonstrated the capacity to transport significant quantities of volume, heat, salt, and potentially biogeochemical properties. However, its pronounced differences to other eddies, such as the PUMP eddy, indicate that each eddy or ITE may exhibit unique features that critically shape its transport dynamics and influence on the surrounding environment. These variations emphasize the importance of studying individual eddies to uncover their specific behaviors and contributions.

While broader patterns can be inferred from the integration of satellite and in situ observations (e.g. Sangrà et al., 2009; Chaigneau et al., 2009; Dong et al., 2014; Pegliasco et al., 2015; Ioannou et al., 2022), detailed, case-specific analyses using high-resolution observational sampling, such as the eIMPACT2 survey, are crucial. Such approaches allow us to capture fine-scale physical processes and provide insights into potential biogeochemical interactions within eddies. This level of detail is

https://doi.org/10.5194/egusphere-2025-99
Preprint. Discussion started: 28 January 2025

required to develop a more comprehensive understanding of the eddies' cumulative impact on regional ocean circulation and biogeochemical cycles.

Future research should prioritize the acquisition of longer-term observational data over broader spatial ranges to advance our understanding of the temporal variability and persistence of these eddies. Such efforts will prove to be essential for enhancing the knowledge base of the dynamics and environmental roles of mesoscale features like the Bentayga eddy.

5 Concluding remarks

This study provides a comprehensive analysis of the ITE Bentayga within the CEC, offering insights into its hydrographic and dynamic properties, zonal transport capabilities, and broader implications for regional oceanography. Using high-resolution data from the eIMPACT2 survey, the study highlights the eddy's complex structure, evolution, and interactions with surrounding mesoscale features.

Bentayga exemplifies the critical role of ITEs in transporting heat, salt, and potentially biogeochemical properties from coastal regions to the ocean interior. A key finding is its intensification during August 2022, as it interacted with upwelling filaments from the northwestern African coast. These filaments not only contributed to the eddy's hydrographic anomalies but also underscored the importance of such coastal-ocean connections in shaping eddy dynamics during their growth phase. This interaction likely enhanced the eddy's capacity for heat and salt transport, further emphasizing the influence of environmental conditions on ITE evolution.

The observed differences between Bentayga and other ITEs, such as the PUMP eddy, illustrate the diversity of these features and the need for case-specific studies to fully understand their behavior and transport dynamics. Bentayga's single-core structure and unique hydrographic profile contrast sharply with PUMP's dual-core configuration, emphasizing the variability in mesoscale eddies' roles within the CEC.

This work provides valuable insights and contributes to a growing body of research on mesoscale eddies, offering a detailed understanding of their role in oceanic processes. However, it also highlights the limitations of generalizing eddy-driven transport based on a single case. Extended high-resolution observational datasets and advanced numerical simulations are needed to capture the full complexity of ITE dynamics, particularly their interactions with surrounding features and external forces like upwelling filaments.

Future efforts should prioritize exploring the variability of these structures over broader temporal and spatial scales, with a focus on the mechanisms driving their intensification and their long-term impacts on ocean circulation, heat and salt fluxes, and ecosystem dynamics.

https://doi.org/10.5194/egusphere-2025-99
Preprint. Discussion started: 28 January 2025

Appendix A: Wavelet analysis of the lagrangnian evolution of the eddy geometric properties of the Bentayga eddy

As previously seen, in Sect. 3.1 (Fig. 3), the geometric properties of the Bentayga eddy reveal significant variability throughout its life cycle, spanning from June 23, 2022, to June 18, 2023. To further investigate the temporal variability and dominant frequencies, a wavelet analysis was conducted (Fig. A1) (Torrence and Compo, 1998).

In this study, a Morlet wavelet was employed, which is well-suited for detecting oscillatory signals and provides good resolution in both time and frequency domains. The dimensionless frequency used was six, which balances the trade-off between time and frequency resolution. The analyzed periods ranged from 4 to 350 days, enabling the detection of both long-term signals and short-term variations.

Figures A1a-c present the wavelet power spectra for amplitude, speed, and radius detrended standardized anomalies, with solid black contours indicating the 90% and 95% significance levels. These significance levels were determined through a Monte Carlo simulation with 10,000 iterations using white noise as a reference for identifying statistically significant fluctuations. The dashed black and white contour represents the cone of influence, which indicates the regions where edge effects reduce the reliability of the results. The global wavelet power spectra, averaged over the entire time series, are shown in Fig. A1d.

The wavelet analysis reveals several dominant periods in all three properties, with significant variability at both low and high frequencies. Remarkably, a strong periodic signal at approximately 256 days (∼8.8 months) is observed for speed and amplitude, corresponding to large-scale seasonal variability during the formation, growth, maturity, and the slow decay phases of the Bentayga eddy, as seen in Fig. 3. The radius shows a similar periodicity, though the peak is less pronounced.

In addition, a secondary peak is observed at shorter periods, around 64 days (∼2 months), indicating higher-frequency fluctuations likely linked to shorter-scale dynamical processes, such as interactions with other mesoscale structures or variations in external forcing (e.g. wind stress). These significant fluctuations, particularly for radius and speed, suggest that the Bentayga eddy experienced intermittent episodes of intensification and relaxation, as reflected in the variability shown in Fig. 3.

The initial rapid growth and transition into the mature phase are captured by shorter-period fluctuations in Figs. A1a-c, where the wavelet power shows more localized variability. However, during the slow decay and the eventual rapid dissipation phase, particularly post-May 2023, the wavelet analysis, using the Morlet wavelet optimized for periodic signals, struggles to resolve these processes fully. This is especially evident in the wavelet's difficulty in resolving the eddy's rapid decay phase. The inherent shape and resolution of the chosen wavelet may smooth out sharp transitions associated with the dissipation of the Bentayga eddy, blending them into longer-period oscillations. Therefore, while the wavelet analysis offers important insights, complementary methods may be needed to fully capture the complete life cycle of the eddy, particularly the rapid transitions at both ends of its evolution.

In summary, the combined results from the time series and wavelet analyses provide a comprehensive picture of the life cycle of the Bentayga eddy, characterized by alternating periods of intensification and decay. External factors, such as interactions with the continental margin and surrounding mesoscale features, likely contributed to these fluctuations, particularly during

https://doi.org/10.5194/egusphere-2025-99
Preprint. Discussion started: 28 January 2025

the early and mature phases. These findings emphasize the importance of multi-scale variability in the life cycle of mesoscale eddies and underscore the need for further investigation into the mechanisms driving these processes.

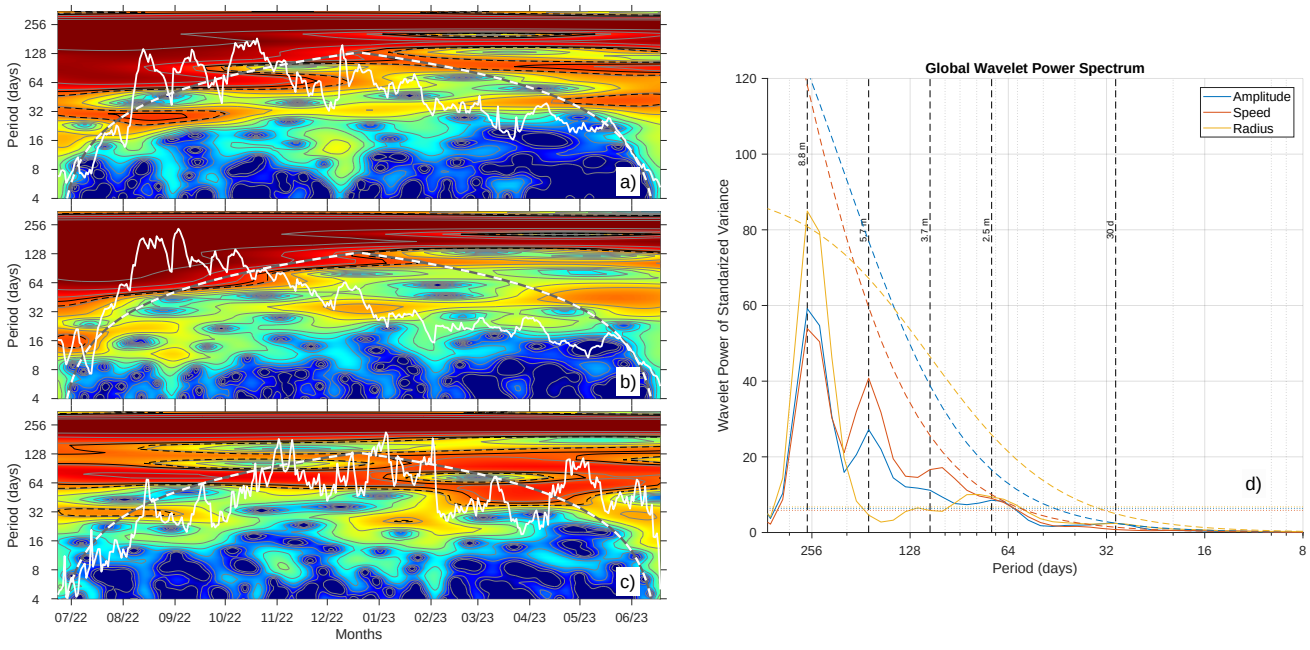

Figure A1. Wavelet analysis of altimetric features exhibited by the Bentayga eddy from the META3.2 NRT product. Panels (a) to (c) display the wavelet power spectrum (colormap) for the detrended standardized anomalies of amplitude, swirl speed, and radius, with thick white lines indicating the corresponding anomalies. Panel (d) illustrates the global wavelet power spectrum, averaged over time. Dashed black/white contours in panels (a) to (c) represent the cone of influence. Also, solid and dashed black contours indicate the 90% and 95% significance levels, determined through a Monte Carlo experiment with 10,000 iterations. Dashed (dotted) lines in panel (d), indicate the 95% red (white) noise levels.

Appendix B: Depth-resolved VMADCP velocity field during eIMPACT2 SeaSoar phase

Figures B1 and B2 present horizontal sections of the velocity field recorded by the VMADCP during the eIMPACT2 SeaSoar phase. The figures group specific depth ranges, with Fig. B1 covering depths from 104 m to 408 m and Fig. B2 showing depths from 472 m to 744 m. These sections illustrate the depth-dependent structure of the circulation within the Bentayga eddy, as well as the potential influence of neighboring eddies.

In the shallow layers (104 m to 248 m), a well-defined and coherent anticyclonic circulation is observed. Between 328 m and 408 m, the eddy core becomes elongated, and signs of a possible bifurcation into dual nuclei are noted at 328 m. This structural change may have resulted from internal deformation of the eddy or interpolation artifacts during data processing.

https://doi.org/10.5194/egusphere-2025-99
Preprint. Discussion started: 28 January 2025

At greater depths (472 m to 744 m), the circulation weakens significantly and becomes increasingly irregular. Although anticyclonic features persist, the influence of external mesoscale eddies appears to dominate, disrupting the eddy's coherence.

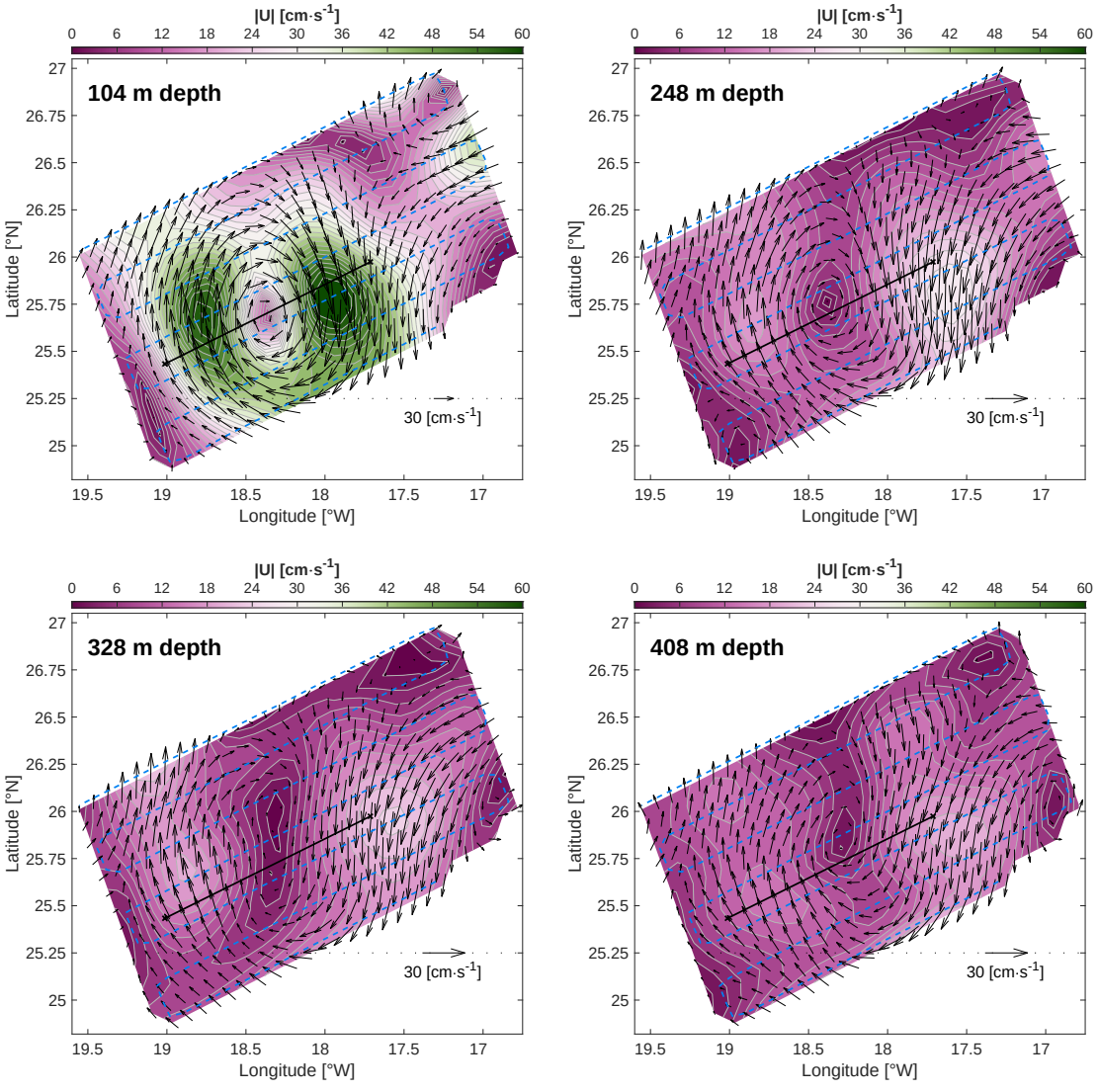

Figure B1. Objectively interpolated VMADCP velocity vectors (black arrows) superimposed on its magnitude contours at various depths: 104, 248, 328, and 408 m. Each panel uses a consistent color scale and speed range with 30 contour levels to highlight the velocity structure. Velocity vectors are scaled proportionally to the respective depth (see legend in the bottom right corner of each panel). The ship's grid-like sampling trajectory during the eIMPACT2 SeaSoar phase (dashed light blue line) and the virtual transect used for the vertical section in Fig. 9 (solid black line) are also indicated. Objective interpolation correlation scales were set to $L_x = L_y = 44$ km, with 3% uncorrelated noise applied.

https://doi.org/10.5194/egusphere-2025-99
Preprint. Discussion started: 28 January 2025

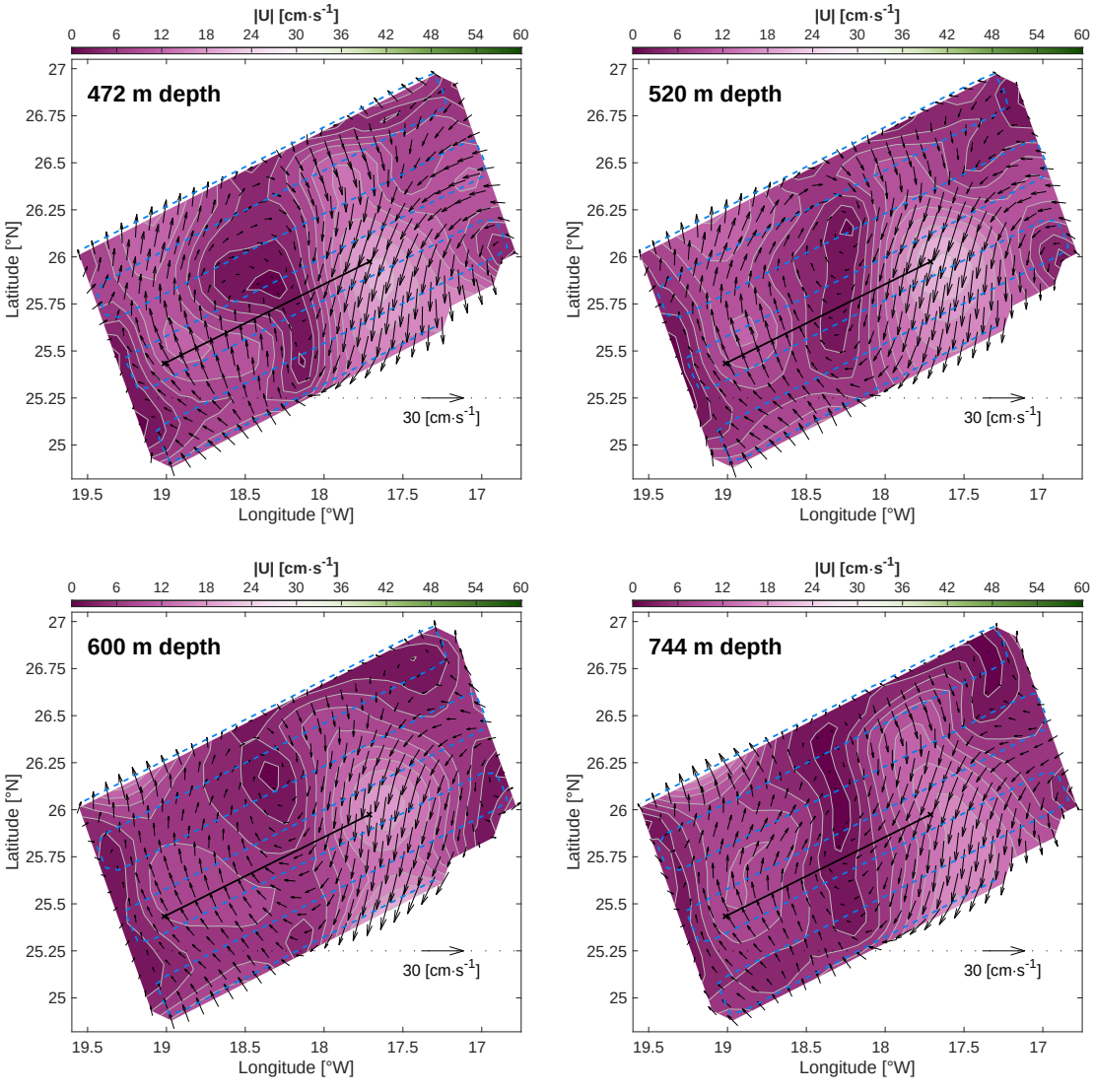

Figure B2. Same as Fig. B1 but for depths: 472, 520, 600, and 744 m.

https://doi.org/10.5194/egusphere-2025-99
Preprint. Discussion started: 28 January 2025

Code availability. The software codes used for the analyses in this study, written in MATLAB, are available upon request from the corresponding author. The specific MATLAB version used for the analyses is R2023b.

Data availability. All in situ data sets used in this study are available upon request from J.A., X.A.Á.S., and A.M.M. The META3.2exp NRT and DT *allsat* products are publicly available and freely distributed by AVISO+ (https://www.aviso.altimetry.fr/). The European Seas Gridded L4 Sea Surface Heights and Derived Variables NRT altimetry product (https://doi.org/10.48670/moi-00142) and the Global Ocean Colour (Copernicus-GlobColour) Bio-Geo-Chemical Level 3 product (https://doi.org/10.48670/moi-00280) are publicly available and freely distributed by the E.U. Copernicus Marine Service Information (CMEMS) (https://marine.copernicus.eu/). The GHRSST Level 4 MUR Global Foundation Sea Surface Temperature Analysis product (https://doi.org/10.5067/GHGMR-4FJ04) is publicly available and freely distributed by PO.DAAC (https://podaac.jpl.nasa.gov/).

Author contributions. L.P.V.: Conceptualization, Investigation, Data Curation, Methodology, Software, Formal Analysis, Validation, Visualization, Writing – Original Draft, and Writing – Review & Editing. Á.R.S.: Conceptualization, Investigation, Methodology, Supervision, Validation, and Writing – Review & Editing. B.A.G.: Methodology, Resources, Software, Formal Analysis, Validation, and Writing – Review & Editing. J.A.: Conceptualization, Investigation, Resources, Project Administration, Funding Acquisition, and Writing – Review & Editing. X.A.Á.: Conceptualization, Investigation, Resources, Project Administration, Funding Acquisition, and Writing – Review & Editing. J.C.: Investigation, Resources, and Writing – Review & Editing. Á.M.M.: Conceptualization, Investigation, Data Curation, Methodology, Supervision, Validation, and Writing – Review & Editing.

Competing interests. The authors declare that they have no conflict of interest.

Acknowledgements. This research was funded by the e-IMPACT project (PID2019-109084RB-C21 and C22) led by J.A. and X.A.Á.S., supported by the Spanish government under the Ministry of Science and Innovation (MCIN/AEI/10.13039/501100011033). L.P.V. acknowledges financial support from the Chilean government through the BECAS CHILE ANID Doctorado en el Extranjero program (Grant No. 72210549) of the National Agency for Research and Development (ANID), under the Ministry of Science, Technology, Knowledge, and Innovation. L.P.V. also expresses gratitude to Bàrbara Barceló-Llull and Francisco Machín for their valuable feedback and insightful discussions throughout the development of this research. Special thanks are extended to the captain and crew of the R/V *Sarmiento de Gamboa*, as well as the Marine Technology Unit (UTM-CSIC) and the scientific staff for their dedicated support during the cruise. To enhance data visualization and promote accessibility for readers with color-vision deficiencies, this study utilized the Scientific color maps (Crameri, 2023) and `cmocean` (Thyng et al., 2016), alongside conventional MATLAB color palettes. These colormaps were selected to prevent visual distortion and improve inclusivity, following best practices in scientific visualization (Crameri et al., 2020). Acknowledgment is given to the use of ChatGPT, developed by OpenAI, for language proofreading and clarity enhancement during the preparation of an earlier draft of this manuscript.

https://doi.org/10.5194/egusphere-2025-99
Preprint. Discussion started: 28 January 2025

References

Alvarez, M., Pérez, F., Shoosmith, D. R., and Bryden, H. L.: Unaccounted role of Mediterranean Water in the drawdown of anthropogenic carbon, Journal of Geophysical Research: Oceans, 110, 1–18, https://doi.org/10.1029/2004JC002633, 2005.

Armi, L. and Zenk, W.: Large Lenses of Highly Saline Mediterranean Water, Journal of Physical Oceanography, 14, 1560–1576, https://doi.org/10.1175/1520-0485(1984)014<1560:LLOHSM>2.0.CO;2, 1984.

Arístegui, J., Sangrà, P., Hernández-León, S., Cantón, M., Hernández-Guerra, A., and Kerling, J. L.: Island-induced eddies in the Canary Islands, Deep-Sea Research I, 41, 1509–1525, https://doi.org/10.1016/0967-0637(94)900058-2, 1994.

Arístegui, J., Tett, P., Hernández-Guerra, A., Basterretxea, G., Montero, M., Wild, K., Sangrá, P., Hernández-Leon, S., Canton, M., García-Braun, J., Pacheco, M., and Barton, E.: The influence of island-generated eddies on chlorophyll distribution: a study of mesoscale variation around Gran Canaria, Deep Sea Research Part I: Oceanographic Research Papers, 44, 71–96, https://doi.org/10.1016/S0967-0637(96)00093-3, 1997.

Aviso+: Mesoscale Eddy Trajectory Atlas Product Handbook META3.2 Delayed Time, https://doi.org/10.24400/527896/a01-2022.005.220209, 2022.

Barceló-Llull, B., Pallàs-Sanz, E., Sangrà, P., Martínez-Marrero, A., Estrada-Allis, S. N., and Arístegui, J.: Ageostrophic secondary circulation in a subtropical intrathermocline eddy, Journal of Physical Oceanography, 47, 1107–1123, https://doi.org/10.1175/JPO-D-16-0235.1, 2017a.

Barceló-Llull, B., Sangrà, P., Pallàs-Sanz, E., Barton, E. D., Estrada-Allis, S. N., Martínez-Marrero, A., Aguiar-González, B., Grisolía, D., Gordo, C., Ángel Rodríguez-Santana, Ángeles Marrero-Díaz, and Arístegui, J.: Anatomy of a subtropical intrathermocline eddy, Deep-Sea Research Part I: Oceanographic Research Papers, 124, 126–139, https://doi.org/10.1016/j.dsr.2017.03.012, 2017b.

Barton, E.: Island Wakes, in: Encyclopedia of Ocean Sciences, edited by Press, E. A., pp. 1397–1403, Elsevier, https://doi.org/10.1006/rwos.2001.0140, 2001.

Barton, E. D., Arístegui, J., Tett, P., Cantón, M., García-Braun, J., Hernández-León, S., Nykjaer, L., Almeida, C., Almunia, J., Ballesteros, S., Basterretxea, G., Escánez, J., García-Weill, L., Hernández-Guerra, A., López-Laatzen, F., Molina, R., Montero, M. F., Navarro-Pérez, E., Rodríguez, J. M., Lenning, K. V., Vélez, H., and Wild, K.: The transition zone of the Canary Current upwelling region, Progress in Oceanography, 41, 455–504, https://doi.org/10.1016/S0079-6611(98)00023-8, 1998.

Barton, E. D., Basterretxea, G., Flament, P., Mitchelson-Jacob, E. G., Jones, B., Arístegui, J., and Herrera, F.: Lee region of Gran Canaria, Journal of Geophysical Research: Oceans, 105, 17 173–17 193, https://doi.org/10.1029/2000jc900010, 2000.

Bashmachnikov, I., Nascimento, A., Neves, F., Menezes, T., and Koldunov, N. V.: Distribution of intermediate water masses in the subtropical northeast Atlantic, Ocean Science, 11, 803–827, https://doi.org/10.5194/os-11-803-2015, 2015.

Basterretxea, G., Barton, E. D., Tett, P., Sangr, P., Navarro-Perez, E., Ar, J., and Istegui, .: Eddy and deep chlorophyl maximum response to wind-shear in the lee of Gran Canaria, Deep-Sea Research I, 49, 1087–1101, https://doi.org/10.1016/S0967-0637(02)00009-2, 2002.

Benítez-Barrios, V. M., Pelegrí, J. L., Hernández-Guerra, A., Lwiza, K. M., Gomis, D., Vélez-Belchí, P., and Hernández-León, S.: Three-dimensional circulation in the NW Africa coastal transition zone, Progress in Oceanography, 91, 516–533, https://doi.org/10.1016/j.pocean.2011.07.022, 2011.

Bosse, A., Testor, P., Mayot, N., Prieur, L., D'Ortenzio, F., Mortier, L., Goff, H. L., Gourcuff, C., Coppola, L., Lavigne, H., and Raimbault, P.: A submesoscale coherent vortex in the Ligurian Sea: From dynamical barriers to biological implications, Journal of Geophysical Research: Oceans, 122, 6196–6217, https://doi.org/10.1002/2016JC012634, 2017.

https://doi.org/10.5194/egusphere-2025-99
Preprint. Discussion started: 28 January 2025

Brannigan, L., Marshall, D. P., Garabato, A. C., Nurser, A. J., and Kaiser, J.: Submesoscale instabilities in mesoscale eddies, Journal of Physical Oceanography, 47, 3061–3085, https://doi.org/10.1175/JPO-D-16-0178.1, 2017.

Bretherton, F. P., Davis, R. E., and Fandry, C. B.: A technique for objective analysis and desing of oceanographic experiments applied to MODE-73, Deep-Sea Research, 23, 559–582, https://doi.org/10.1016/0011-7471(76)90001-2, 1976.

Bretherton, F. P., McPhade, M. J., and Kraus, E. B.: Design studies for Climatological Measurements of Heat Storage, Journal of Physical Oceanography, 14, 318–337, https://doi.org/10.1175/1520-0485(1984)014<0318:DSFCMO>2.0.CO;2, 1984.

Caldeira, R. M., Stegner, A., Couvelard, X., Araújo, I. B., Testor, P., and Lorenzo, A.: Evolution of an oceanic anticyclone in the lee of Madeira Island: In situ and remote sensing survey, Journal of Geophysical Research: Oceans, 119, 1195–1216, https://doi.org/10.1002/2013JC009493, 2014.

Candela, J., Beardsley, R. C., and Limeburner, R.: Separation of tidal and subtidal currents in ship-mounted acoustic Doppler current profiler observations, Journal of Geophysical Research, 97, 769–788, https://doi.org/10.1029/91JC02569, 1992.

Cardoso, C., Caldeira, R. M., Relvas, P., and Stegner, A.: Islands as eddy transformation and generation hotspots: Cabo Verde case study, Progress in Oceanography, 184, https://doi.org/10.1016/j.pocean.2020.102271, 2020.

Cerdán-García, E., Álvarez Salgado, X. A., Arístegui, J., Martínez-Marrero, A., and Benavides, M.: Eddy-driven diazotroph distribution in the subtropical North Atlantic: horizontal variability prevails over particle sinking speed, Communications Biology, 7, https://doi.org/10.1038/s42003-024-06576-w, 2024.

Chaigneau, A., Eldin, G., and Dewitte, B.: Eddy activity in the four major upwelling systems from satellite altimetry (1992-2007), Progress in Oceanography, 83, 117–123, https://doi.org/10.1016/j.pocean.2009.07.012, 2009.

Chaigneau, A., Texier, M. L., Eldin, G., Grados, C., and Pizarro, O.: Vertical structure of mesoscale eddies in the eastern South Pacific Ocean: A composite analysis from altimetry and Argo profiling floats, Journal of Geophysical Research: Oceans, 116, https://doi.org/10.1029/2011JC007134, 2011.

Chelton, D. B., deSzoeke, R. A., Schlax, M. G., Naggar, K. E., and Siwertz, N.: Geographical Variability of the First Baroclinic Rossby Radius of Deformation, Journal of Physical Oceanography, 28, 433 – 460, https://doi.org/10.1175/1520-0485(1998)028<0433:GVOTFB>2.0.CO;2, 1998.

Chelton, D. B., Schlax, M. G., Samelson, R. M., and de Szoeke, R. A.: Global observations of large oceanic eddies, Geophysical Research Letters, 34, 1–5, https://doi.org/10.1029/2007GL030812, 2007.

Chelton, D. B., Gaube, P., Schlax, M. G., Early, J. J., and Samelson, R. M.: Global observations of nonlinear mesoscale eddies, Progress in Oceanography, 91, 167–216, https://doi.org/10.1016/j.pocean.2011.01.002, 2011.

Chin, T. M., Vazquez-Cuervo, J., and Armstrong, E. M.: A multi-scale high-resolution analysis of global sea surface temperature ☆, Remote Sensing of Environment, https://doi.org/10.1016/j.rse.2017.07.029, 2017.

Chopra, K. and Hubert, L.: Mesoscale Eddies in Wake of Islands, Journal of Atmospheric Sciences, 22, 652–657, https://doi.org/10.1175/1520-0469(1965)022<0652:MEIWOI>2.0.CO;2, 1965.

Chopra, K. P.: Atmospheric and Oceanic Flow Problems Introduced By Islands, VIMS Contribution No. 489., in: Advances in Geophysics, edited by Landsberg, H. and Van Mieghem, J., vol. 16, pp. 297–421, Elsevier, https://doi.org/10.1016/S0065-2687(08)60354-4, 1973.

Contreras, M., Pizarro, O., Dewitte, B., Sepulveda, H. H., and Renault, L.: Subsurface Mesoscale Eddy Generation in the Ocean off Central Chile, Journal of Geophysical Research: Oceans, 124, 5700–5722, https://doi.org/10.1029/2018JC014723, 2019.

https://doi.org/10.5194/egusphere-2025-99
Preprint. Discussion started: 28 January 2025

Cornejo D'Ottone, M., Bravo, L., Ramos, M., Pizarro, O., Karstensen, J., Gallegos, M., Correa-Ramirez, M., Silva, N., Farias, L., and Karp-Boss, L.: Biogeochemical characteristics of a long-lived anticyclonic eddy in the eastern South Pacific Ocean, Biogeosciences, 13, 2971–2979, https://doi.org/10.5194/bg-13-2971-2016, 2016.

Crameri, F.: Scientific colour maps, https://doi.org/10.5281/zenodo.8409685, 2023.

Crameri, F., Shephard, G. E., and Heron, P. J.: The misuse of colour in science communication, Nature Communications, 11, 5444, https://doi.org/10.1038/s41467-020-19160-7, 2020.

de Marez, C., Carton, X., L'Hégaret, P., Meunier, T., Stegner, A., Vu, B. L., and Morvan, M.: Oceanic vortex mergers are not isolated but influenced by the β-effect and surrounding eddies, Scientific Reports, 10, https://doi.org/10.1038/s41598-020-59800-y, 2020.

Dilmahamod, A. F., Aguiar-González, B., Penven, P., Reason, C. J., Ruijter, W. P. D., Malan, N., and Hermes, J. C.: SIDDIES Corridor: A Major East-West Pathway of Long-Lived Surface and Subsurface Eddies Crossing the Subtropical South Indian Ocean, Journal of Geophysical Research: Oceans, 123, 5406–5425, https://doi.org/10.1029/2018JC013828, 2018.

Dilmahamod, A. F., Karstensen, J., Dietze, H., Löptien, U., and Fennel, K.: Generation Mechanisms of Mesoscale Eddies in the Mauritanian Upwelling Region, Journal of Physical Oceanography, 52, 161–182, https://doi.org/10.1175/JPO-D-21-0092.1, 2022.

Djurfeldt, L.: Circulation and mixing in a coastal upwelling embayment; Gulf of Arauco, Chile, Continental Shelf Research, 9, 1003–1016, https://doi.org/10.1016/0278-4343(89)90004-6, 1989.

Dong, C., McWilliams, J. C., Liu, Y., and Chen, D.: Global heat and salt transports by eddy movement, Nature Communications, 5, https://doi.org/10.1038/ncomms4294, 2014.

Dugan, J. P., Mied, R. P., Mignerey, P. C., and Schuetz, A. F.: Compact, intrathermocline eddies in the Sargasso Sea, Journal of Geophysical Research: Oceans, 87, 385–393, https://doi.org/10.1029/JC087iC01p00385, 1982.

Estrada-Allis, S. N., Barceló-Llull, B., Pallàs-Sanz, E., Rodríguez-Santana, A., Souza, J. M., Mason, E., Mcwilliams, J. C., and Sangrà, P.: Vertical velocity dynamics and mixing in an anticyclone near the Canary Islands, Journal of Physical Oceanography, 49, 431–451, https://doi.org/10.1175/JPO-D-17-0156.1, 2019.

Feistel, R.: A new extended Gibbs thermodynamic potential of seawater, Progress in Oceanography, 58, 43–114, https://doi.org/10.1016/S0079-6611(03)00088-0, 2003.

Feistel, R.: A Gibbs function for seawater thermodynamics for -6 to 80°C and salinity up to 120gkg–1, Deep Sea Research Part I: Oceanographic Research Papers, 55, 1639–1671, https://doi.org/10.1016/j.dsr.2008.07.004, 2008.

Fernández-Castro, B., Evans, D. G., Frajka-Williams, E., Vic, C., and Naveira-Garabato, A. C.: Breaking of internal waves and turbulent dissipation in an anticyclonic mode water eddy, Journal of Physical Oceanography, 50, 1893–1914, https://doi.org/10.1175/JPO-D-19-0168.1, 2020.

Fu, M., Dong, C., Dong, J., and Sun, W.: Analysis of Mesoscale Eddy Merging in the Subtropical Northwest Pacific Using Satellite Remote Sensing Data, Remote Sensing, 15, https://doi.org/10.3390/rs15174307, 2023.

Garnesson, P., Mangin, A., d'Andon, O. F., Demaria, J., and Bretagnon, M.: The CMEMS GlobColour chlorophyll a product based on satellite observation: Multi-sensor merging and flagging strategies, Ocean Science, 15, 819–830, https://doi.org/10.5194/os-15-819-2019, 2019.

Gordon, A. L., Giulivi, C. F., Lee, C. M., Hunt, H., Bower, A., and Talley, L.: Japan/East Sea Intrathermocline Eddies, Journal of Physical Oceanography, 32, 1960–1974, https://doi.org/10.1175/1520-0485(2002)032<1960:JESIE>2.0.CO;2, 2002.

Hebert, D.: The available potential energy of an isolated feature, Journal of Geophysical Research: Oceans, 93, 556–564, https://doi.org/10.1029/jc093ic01p00556, 1988.

https://doi.org/10.5194/egusphere-2025-99
Preprint. Discussion started: 28 January 2025

Hebert, D., Oakey, N., and Ruddick, B.: Evolution of a Mediterranean Salt Lens: Scalar Properties, Journal of Physical Oceanography, 20, 1468–1483, https://doi.org/10.1175/1520-0485(1990)020<1468:EOAMSL>2.0.CO;2, 1990.

Hernández-Guerra, A., Arístegui, A., Cantón, M., and Nykjaer, L.: Phytoplankton pigment patterns in the canary islands area as determined using coastal zone colour scanner data, International Journal of Remote Sensing, 14, 1431–1437, https://doi.org/10.1080/01431169308953977, 1993.

Hernández-Hernández, N., Arístegui, J., Montero, M. F., Velasco-Senovilla, E., Baltar, F., Ángeles Marrero-Díaz, Martínez-Marrero, A., and Ángel Rodríguez-Santana: Drivers of Plankton Distribution Across Mesoscale Eddies at Submesoscale Range, Frontiers in Marine Science, 7, https://doi.org/10.3389/fmars.2020.00667, 2020.

Hogan, P. J. and Hurlburt, H. E.: Why do Intrathermocline Eddies form in the Japan/East Sea? A Modeling Perspective, Oceanography, 19, 134–143, https://doi.org/10.5670/oceanog.2006.50, 2006.

Hormazabal, S., Combes, V., Morales, C. E., Correa-Ramirez, M. A., Lorenzo, E. D., and Nuñez, S.: Intrathermocline eddies in the coastal transition zone off central Chile (31-41°S), Journal of Geophysical Research: Oceans, 118, 4811–4821, https://doi.org/10.1002/jgrc.20337, 2013.

Ioannou, A., Speich, S., and Laxenaire, R.: Characterizing Mesoscale Eddies of Eastern Upwelling Origins in the Atlantic Ocean and Their Role in Offshore Transport, Frontiers in Marine Science, 9, https://doi.org/10.3389/fmars.2022.835260, 2022.

Jiménez, B., Sangrà, P., and Mason, E.: A numerical study of the relative importance of wind and topographic forcing on oceanic eddy shedding by tall, deep water islands, Ocean Modelling, 22, 146–157, https://doi.org/10.1016/j.ocemod.2008.02.004, 2008.

Jiménez-Rincón, J. A., Cianca, A., Ferrero-Martín, C., and Izquierdo, A.: A Glider View of the Spreading and Mixing Processes of Antarctic Intermediate Water in the Northeastern Subtropical Atlantic, Journal of Marine Science and Engineering, 11, https://doi.org/10.3390/jmse11030576, 2023.

Johnson, G. C. and Mctaggart, K. E.: Equatorial pacific 13°c water eddies in the eastern subtropical south pacific ocean, Journal of Physical Oceanography, 40, 226–236, https://doi.org/10.1175/2009JPO4287.1, 2010.

Karstensen, J., Schütte, F., Pietri, A., Krahmann, G., Fiedler, B., Grundle, D., Hauss, H., Körtzinger, A., Löscher, C. R., Testor, P., Vieira, N., and Visbeck, M.: Upwelling and isolation in oxygen-depleted anticyclonic modewater eddies and implications for nitrate cycling, Biogeosciences, 14, 2167–2181, https://doi.org/10.5194/bg-14-2167-2017, 2017.

Kolodziejczyk, N., Testor, P., Lazar, A., Echevin, V., Krahmann, G., Chaigneau, A., Gourcuff, C., Wade, M., Faye, S., Estrade, P., Capet, X., Mortier, L., Brehmer, P., Schütte, F., and Karstensen, J.: Subsurface Fine-Scale Patterns in an Anticyclonic Eddy Off Cap-Vert Peninsula Observed From Glider Measurements, Journal of Geophysical Research: Oceans, 123, 6312–6329, https://doi.org/10.1029/2018JC014135, 2018.

Kostianoy, A. and Belkin, I.: A Survey of Observations on Intrathermocline Eddies in the World Ocean, in: Mesoscale/Synoptic Coherent structures in Geophysical Turbulence, edited by Nihoul, J. and Jamart, B., vol. 50 of *Elsevier Oceanography Series*, pp. 821–841, Elsevier, https://doi.org/https://doi.org/10.1016/S0422-9894(08)70223-X, 1989.

La Violette, P. E.: A Satellite-Aircraft Thermal Study of the Upwelled Waters off Spanish Sahara, Journal of Physical Oceanography, 4, 676–684, https://doi.org/10.1175/1520-0485(1974)004<0676:ASATSO>2.0.CO;2, 1974.

Le Traon, P. Y.: A Method for Optimal Analysis of Fields with Spatially Variable Mean, Journal of Geophysical Research, 95, 13 543–13 547, https://doi.org/10.1029/JC095iC08p13543, 1990.

Machín, F. J. and Pelegrí, J. L.: Interacción de remolinos de agua Mediterránea con agua intermedia Antártica al noroeste de África, Scientia Marina, 80, 205–214, https://doi.org/10.3989/scimar.04289.06A, 2016.

https://doi.org/10.5194/egusphere-2025-99
Preprint. Discussion started: 28 January 2025

Marchesiello, P. and Estrade, P.: Eddy activity and mixing in upwelling systems: A comparative study of Northwest Africa and California, International Journal of Earth Sciences, 98, 299–308, https://doi.org/10.1007/s00531-007-0235-6, 2009.

Martínez-Marrero, A., Barceló-Llull, B., Pallàs-Sanz, E., Aguiar-González, B., Estrada-Allis, S. N., Gordo, C., Grisolía, D., Rodríguez-Santana, A., and Arístegui, J.: Near-Inertial Wave Trapping Near the Base of an Anticyclonic Mesoscale Eddy Under Normal Atmospheric Conditions, Journal of Geophysical Research: Oceans, 124, 8455–8467, https://doi.org/10.1029/2019JC015168, 2019.

Mason, E., Pascual, A., and McWilliams, J. C.: A new sea surface height-based code for oceanic mesoscale eddy tracking, Journal of Atmospheric and Oceanic Technology, 31, 1181–1188, https://doi.org/10.1175/JTECH-D-14-00019.1, 2014.

Mcgillicuddy, D. J.: Formation of intrathermocline lenses by eddy-wind interaction, Journal of Physical Oceanography, 45, 606–612, https://doi.org/10.1175/JPO-D-14-0221.1, 2015.

McWilliams, J. C.: Submesoscale, Coherent Vortices in the Ocean, Reviews of Geophysics, 23, 165–182, https://doi.org/10.1029/RG023i002p00165, 1985.

Molemaker, M. J., Mcwilliams, J. C., and Dewar, W. K.: Submesoscale instability and generation of mesoscale anticyclones near a separation of the California undercurrent, Journal of Physical Oceanography, 45, 613–629, https://doi.org/10.1175/JPO-D-13-0225.1, 2015.

Morris, T., Aguiar-González, B., Ansorge, I., and Hermes, J.: Lagrangian Evolution of Two Madagascar Cyclonic Eddies: Geometric Properties, Vertical Structure, and Fluxes, Journal of Geophysical Research: Oceans, 124, 8193–8218, https://doi.org/10.1029/2019JC015090, 2019.

Müller, P.: Ertel's potential vorticity theorem in physical oceanography, Reviews of Geophysics, 33, 67–97, https://doi.org/10.1029/94RG03215, 1995.

Nauw, J. J., van Aken, H. M., Lutjeharms, J. R., and de Ruijter, W. P.: Intrathermocline eddies in the Southern Indian Ocean, Journal of Geophysical Research: Oceans, 111, https://doi.org/10.1029/2005JC002917, 2006.

Pacheco, M., García-Weil, L., Rodríguez, G. R., Tejera, A., and Luque, A.: Upwelling Filaments in the Northwest African Coastal Transition Zone (NACTZ); Satellite Images and Laboratory Simulations, in: IGARSS 2001. Scanning the Present and Resolving the Future. Proceedings. IEEE 2001 International Geoscience and Remote Sensing Symposium (Cat. No.01CH37217), pp. 3015–3017, https://doi.org/10.1109/IGARSS.2001.978239, 2001.

Pegliasco, C., Chaigneau, A., and Morrow, R.: Main eddy vertical structures observed in the four major Eastern Boundary Upwelling Systems, Journal of Geophysical Research: Oceans, 120, 6008–6033, https://doi.org/10.1002/2015JC010950, 2015.

Pegliasco, C., Delepoulle, A., Mason, E., Morrow, R., Faugère, Y., and Dibarboure, G.: META3.1exp: a new global mesoscale eddy trajectory atlas derived from altimetry, Earth System Science Data, 14, 1087–1107, https://doi.org/10.5194/essd-14-1087-2022, 2022.

Pelegrí, J. L., Arístegui, J., Cana, L., González-Dávila, M., Hernández-Guerra, A., Hernández-León, S., Marrero-Díaz, A., Montero, M. F., Sangrà, P., and Santana-Casiano, M.: Coupling between the open ocean and the coastal upwelling region off northwest Africa: Water recirculation and offshore pumping of organic matter, Journal of Marine Systems, 54, 3–37, https://doi.org/10.1016/j.jmarsys.2004.07.003, 2005.

Pidcock, R., Martin, A., Allen, J., Painter, S. C., and Smeed, D.: The spatial variability of vertical velocity in an Iceland basin eddy dipole, Deep-Sea Research Part I: Oceanographic Research Papers, 72, 121–140, https://doi.org/10.1016/j.dsr.2012.10.008, 2013.

Piedeleu, M., Sangra, P., Sánchez-Vidal, A., Fabrés, J., Gordo, C., and Calafat, A.: An observational study of oceanic eddy generation mechanisms by tall deep-water islands (Gran Canaria), Geophysical Research Letters, 36, https://doi.org/10.1029/2008GL037010, 2009.

https://doi.org/10.5194/egusphere-2025-99
Preprint. Discussion started: 28 January 2025

Pingree, R. and Garcia-Soto, C.: Annual westward propagating anomalies near 26°N and eddy generation south of the Canary Islands: Remote sensing (altimeter/SeaWiFS) and in situ measurement, Journal of the Marine Biological Association of the United Kingdom, 84, 1105–1115, https://doi.org/10.1017/S0025315404010549h, 2004.

Pingree, R. D.: A Shallow Subtropical Subducting Westward Propagating Eddy (Swesty), Philosophical Transactions: Mathematical, Physical and Engineering Sciences, 354, 979–1026, https://doi.org/10.1098/rsta.1996.0039, 1996.

Prater, M. D. and Sanford, T. B.: A Meddy off Cape St. Vincent. Part I: Description, Journal of Physical Oceanography, 24, 1572–1586, https://doi.org/10.1175/1520-0485(1994)024<1572:AMOCSV>2.0.CO;2, 1994.

Richardson, P. L., Walsh, D., Armi, L., Schröder, M., and Price, J. F.: Tracking Three Meddies with SOFAR Floats, Journal of Physical Oceanography, 19, 371–382, https://doi.org/10.1175/1520-0485(1989)019<0371:TTMWSF>2.0.CO;2, 1989.

Richardson, P. L., Bower, A. S., and Zenk, W.: A census of Meddies tracked by floats, Progress in Oceanography, 45, 209–250, https://doi.org/10.1016/S0079-6611(99)00053-1, 2000.

Rodríguez-Marroyo, R., Álvaro Viúdez, and Ruiz, S.: Vortex merger in oceanic tripoles, Journal of Physical Oceanography, 41, 1239–1251, https://doi.org/10.1175/2011JPO4582.1, 2011.

Ruddick, B. and Hebert, D.: The Mixing of Meddy "Sharon", in: Small Scale Turbulence and Mixing in the Ocean, edited by Nihoul, J. and Jamart, B., vol. 46, pp. 249–261, Elsevier Oceanography Series, https://doi.org/10.1016/S0422-9894(08)70551-8, 1988.

Rudnick, D. L. and Luyten, J. R.: Intensive surveys of the Azores Front 1. Tracers and dynamics, Journal of Geophysical Research: Oceans, 101, 923–939, https://doi.org/10.1029/95JC02867, 1996.

Ruiz, S., Pelegrí, J. L., Emelianov, M., Pascual, A., and Mason, E.: Geostrophic and ageostrophic circulation of a shallow anticyclonic eddy off Cape Bojador, Journal of Geophysical Research: Oceans, 119, 1257–1270, https://doi.org/10.1002/2013JC009169, 2014.

Rykova, T. and Oke, P. R.: Stacking of EAC Eddies Observed From Argo, Journal of Geophysical Research: Oceans, 127, https://doi.org/10.1029/2022JC018679, 2022.

Sangrà, P., Pelegrí, J. L., Hernández-Guerra, A., Arregui, I., Martín, J. M., Marrero-Díaz, A., Martínez, A., Ratsimandresey, A. W., and Rodríguez-Santana, A.: Life history of an anticyclonic eddy, Journal of Geophysical Research: Oceans, 110, 1–19, https://doi.org/10.1029/2004JC002526, 2005.

Sangrà, P., Auladell, M., Marrero-Díaz, A., Pelegrí, J. L., Fraile-Nuez, E., Rodríguez-Santana, A., Martín, J. M., Mason, E., and Hernández-Guerra, A.: On the nature of oceanic eddies shed by the Island of Gran Canaria, Deep-Sea Research Part I: Oceanographic Research Papers, 54, 687–709, https://doi.org/10.1016/j.dsr.2007.02.004, 2007.

Sangrà, P., Pascual, A., Ángel Rodríguez-Santana, Machín, F., Mason, E., McWilliams, J. C., Pelegrí, J. L., Dong, C., Rubio, A., Arístegui, J., Ángeles Marrero-Díaz, Hernández-Guerra, A., Martínez-Marrero, A., and Auladell, M.: The Canary Eddy Corridor: A major pathway for long-lived eddies in the subtropical North Atlantic, Deep-Sea Research Part I: Oceanographic Research Papers, 56, 2100–2114, https://doi.org/10.1016/j.dsr.2009.08.008, 2009.

Schmid, C., Schäfer, H., Guillermo, P., and Zenk, W.: The Vitória Eddy and Its Relation to the Brazil Current, Journal of Physical Oceanography, 25, 2532–2546, https://doi.org/10.1175/1520-0485(1995)025<2532:TVEAIR>2.0.CO;2, 1995.

Schultz Tokos, K. and Rossby, T.: Kinematics and Dynamics of a Mediterranean Salt Lens, Journal of Physical Oceanography, 21, 879–892, https://doi.org/10.1175/1520-0485(1991)021<0879:KADOAM>2.0.CO;2, 1991.

Schütte, F., Brandt, P., and Karstensen, J.: Occurrence and characteristics of mesoscale eddies in the tropical northeastern Atlantic Ocean, Ocean Science, 12, 663–685, https://doi.org/10.5194/os-12-663-2016, 2016.

https://doi.org/10.5194/egusphere-2025-99
Preprint. Discussion started: 28 January 2025

Shapiro, G. I. and Meschanov, S. L.: Distribution and spreading of Red Sea Water and salt lens formation in the northwest Indian Ocean, Deep-Sea Research, 38, 21–34, https://doi.org/10.1016/0198-0149(91)90052-H, 1991.

Thomas, L. N.: Formation of intrathermocline eddies at ocean fronts by wind-driven destruction of potential vorticity, Dynamics of Atmospheres and Oceans, 45, 252–273, https://doi.org/10.1016/j.dynatmoce.2008.02.002, 2008.

Thomsen, S., Kanzow, T., Krahmann, G., Greatbatch, R. J., Dengler, M., and Lavik, G.: The formation of a subsurface anticyclonic eddy in the Peru-Chile Undercurrent and its impact on the near-coastal salinity, oxygen, and nutrient distributions, Journal of Geophysical Research: Oceans, 121, 476–501, https://doi.org/10.1002/2015JC010878, 2016.

Thyng, K. M., Greene, C. A., Hetland, R. D., Zimmerle, H. M., and DiMarco, S. F.: True Colors of Oceanography: Guidelines for Effective and Accurate Colormap Selection, Oceanography, 29, 9–13, http://www.jstor.org/stable/24862699, 2016.

Tomczak, M. and Godfrey, J. S.: Regional Oceanography: An Introduction, Daya Publishing House, Delhi, India, 2nd edn., ISBN 8170353068, 2004.

Torrence, C. and Compo, G. P.: A Practical Guide to Wavelet Analysis, Bulletin of the American Meteorological Society, 79, 61 – 78, https://doi.org/10.1175/1520-0477(1998)079<0061:APGTWA>2.0.CO;2, 1998.

Van Camp, L., Nykjier, L., Mittelstaedt, E., and Schlittenhardt, P.: Upwelling and boundary circulation off Northwest Africa as depicted by infrared and visible satellite observations, Progress in Oceanography, 26, 357–402, https://doi.org/10.1016/0079-6611(91)90012-B, 1991.